Journal of Geophysical Research: Planets

RESEARCH ARTICLE
10.1029/2018JE005665

Special Section:
Planetary Mapping: Methods, Tools for Scientific Analysis and Exploration

# Grid Mapping the Northern Plains of Mars: Using Morphotype and Distribution of Ice-Related Landforms to Understand Multiple Ice-Rich Deposits in Utopia Planitia

**Antoine Séjourné[1], Francois Costard[1], Zuzanna M. Swirad[2], Anna Łosiak[3,4], Sylvain Bouley[1], Isaac Smith[5,6], Matthew R. Balme[7], Csilla Orgel[8,9], Jason D. Ramsdale[7], Ernst Hauber[9], Susan J. Conway[7,10], Stephan van Gasselt[8,11], Dennis Reiss[12], Andreas Johnsson[13], Colman Gallagher[14,15], James A. Skinner[16], Ákos Kereszturi[17], and Thomas Platz[8,18]**

[1]GEOPS, Université Paris-Sud, CNRS, Université Paris-Saclay, Orsay, France, [2]Department of Geography, Durham University, Durham, UK, [3]Institute of Geological Sciences, Polish Academy of Sciences, Wrocław, Poland, [4]WildFIRE Lab, University of Exeter, Exeter, UK, [5]Lassonde School of Engineering, York University, Toronto, Ontario, Canada, [6]Planetary Science Institute, Lakewood, CO, USA, [7]Department of Physical Sciences, Open University, Milton Keynes, UK, [8]Institute of Geological Sciences, Planetary Sciences and Remote Sensing, Freie Universität Berlin, Berlin, Germany, [9]DLR-Institut für Planetenforschung, Berlin, Germany, [10]Laboratoire de Planétologie et Géodynamique—UMR CNRS 6112, Nantes, France, [11]Department of Land Economics, National Chengchi University, Taipei, Taiwan, [12]Institut für Planetologie, Westfälische Wilhelms-Universität, Münster, Germany, [13]Department of Earth Sciences, University of Gothenburg, Gothenburg, Sweden, [14]UCD School of Geography, University College, Dublin, Ireland, [15]UCD Earth Institute, University College, Dublin, Ireland, [16]USGS Astrogeology Science Center, Flagstaff, AZ, USA, [17]Konkoly Observatory, Research Centre for Astronomy and Earth Sciences, Hungarian Academy of Sciences, Budapest, Hungary, [18]Max Planck Institut für Sonnensystemforschung, Göttingen, Germany

**Abstract** This work in Utopia Planitia is the first continuous regional mapping of ice-related landforms integrated into an effort to study the three main basins (Arcadia, Acidalia, and Utopia Planitiae) in the northern plains. The distribution and morphotypes of these landforms, SHAllow RADar detections, and crater size-frequency distribution measurements (>50 m in diameter) were used to understand the permafrost cryolithology and its past evolution in relation to climate in Utopia Planitia. Three assemblages of landforms were identified based on their spatial correlation and correlation with Mars Orbiter Laser Altimeter surface roughness along a strip from 30°N to 80°N. At 30°–38°N, the assemblage is formed by kilometer-scale polygons, high-albedo mounds, and thumbprint terrains. This assemblage is associated with a lobate deposit of 30 m in thickness with a crater retention age of 1 Ga. At 38°–47°N, the assemblage is comprised of large scallops, 100-m-diameter polygons, pits, and mantled deposits. This assemblage is correlated with a deposit of 80 m in thickness containing excess ice (~50–85% by volume) with a crater retention age of about 10 Ma. At 47°–78°N, the assemblage is composed of mantled deposits, textured terrains, and 30-m-diameter polygons. This assemblage is related to the ice-rich, debris-covered, latitude-dependent mantle that has a crater retention age of about 1.5 Ma. Utopia Planitia appears to be a region of combined depositions of sediment and continuous cold climatic conditions that leaded to a complex distribution of ground ice.

**Plain Language Summary** The northern plains of Mars comprise several basins filled by sediments. The region has been proposed to have hosted an ancient ocean and currently contains ice in the ground even at latitudes where the ice is not stable. It is not known, however, what is the origin of the ice, whether it is related to the ancient ocean or recent glaciations. The ages of different surfaces and landforms are also not well known. Improving the geological context of the northern plains will help constrain outstanding questions about evolution of the climate and geology on Mars. An International Space Science Institute team project, composed of several European laboratories with expertise in mapping, has been convened to study targeted areas in the northern plain of Mars. In Utopia Planitia, we mapped and used the distribution of ice-related landforms and radar sounding to understand the distribution of ice over the region. Two young ice-rich deposits with different ice content were identified over the middle and high latitudes of the region. Similar to some regions in the Arctic on Earth, Utopia Planitia appears to be a region of combined deposition of sediment and continuous cold climatic conditions that partially preserved several ice-rich deposits.

This article is a companion to Ramsdale et al. (2018), https://doi.org/10.1029/2018JE005663; Orgel et al. (2018), https://doi.org/10.1029/2018JE005664.

**Key Points:**
- Distribution and morphotype of ice-related landforms were used to understand the permafrost cryolithology and evolution in Utopia Planitia
- A midlatitude, ice-rich, stratified permafrost (50–85% by volume) of 11-Ma age occurs from 38°N to 47°N
- The latitude-dependent mantle of about 1.5-Ma age is present from 47°N to 78°N

**Supporting Information:**
- Supporting Information S1
- Figure S1
- Figure S2
- Figure S3
- Figure S4

**Correspondence to:**
A. Séjourné,
antoine.sejourne@u-psud.fr

**Citation:**
Séjourné, A., Costard, F., Swirad, Z. M., Łosiak, A., Bouley, S., Smith, I., et al. (2019). Grid mapping the northern plains of Mars: Using morphotype and distribution of ice-related landforms to understand multiple ice-rich deposits in Utopia Planitia. *Journal of Geophysical Research: Planets*, *124*, 483–503. https://doi.org/10.1029/2018JE005665

Received 1 MAY 2018
Accepted 7 SEP 2018
Accepted article online 13 SEP 2018
Published online 21 FEB 2019

## 1. Introduction

The northern plains of Mars, topographically lower than the southern cratered highlands, comprise several large basins that are variably filled by materials stratigraphically younger than the highlands (e.g., Baker et al., 1991; Kreslavsky & Head, 2002a). Many landforms found in the northern plains are indicative of ground ice, including debris-covered glaciers referred to as viscous flow features (VFF; Carr, 2001; Squyres, 1978), scalloped depressions (e.g., Costard & Kargel, 1995; Morgenstern et al., 2007; Séjourné et al., 2011), thermal contraction polygons (e.g., Mangold, 2005; Seibert & Kargel, 2001), and gullies (Malin & Edgett, 2000). Presence of subsurface ground ice at high latitudes has been confirmed by spectral measurements of hydrogen abundance (e.g., Feldman et al., 2004) and by direct observations from the Phoenix lander (Mellon et al., 2009). Its distribution is correlated with the current near-surface ground ice stability for latitudes $>60°$ (Haberle et al., 2003; Mellon & Jakosky, 1995). Ground ice at a depth greater than 1 m has been detected by direct observations of fresh craters (Byrne et al., 2009) and sublimation depressions (Dundas et al., 2018), as well as by radar sounding (Mouginot et al., 2012; Plaut et al., 2009).

However, no consensus has emerged as to what process was responsible for the presence of ground ice in the northern plains. During the Hesperian, these lowlands may have been the location of accumulation and later freezing of sediments from multiple episodes of outflow channel discharge and perhaps even from a large ocean (e.g., Baker et al., 1991; Carr & Head, 2003; Clifford & Parker, 2001; Parker et al., 1993). During the Amazonian, significant variations in the orbital parameters are thought to have induced cyclic accumulations of ice in different areas of the northern plains. Variations in obliquity and eccentricity control the pattern of insolation and, thus, the climate (e.g., Chamberlain & Boynton, 2007; Haberle et al., 2003; Laskar et al., 2004; Mellon & Jakosky, 1995).

An ice-rich and geologically young (0.4–2.1 Ma) latitude-dependent mantle (LDM) is present and smooths the topography at latitudes $>30°$ in both hemispheres (Head et al., 2003; Mustard et al., 2001). Climatic models have simulated the formation of the LDM from ice deposition during periods of low or moderate obliquity suggesting a link with climate changes due to orbital cycles (Forget et al., 2006; Haberle et al., 2003; Head et al., 2003; Levrard et al., 2004; Mischna et al., 2003).

Moreover, along the dichotomy between the southern highlands and the northern plains (specifically from 30° to 50°N), VFF are interpreted to represent the remnants of glaciation formed during the Late Amazonian (Carr, 2001; Hauber et al., 2005; Head et al., 2006, 2010; Mangold, 2005). These glacial features could have been formed by ice deposition during moderate-obliquity periods (Head et al., 2006; Madeleine et al., 2009). Additionally, other ice-rich mantles were identified in multiple northern lowland locations and possibly predating the LDM (Kadish & Head, 2014; Kargel et al., 1995).

Improving the geological context of the northern plains will help improve our understanding of the recent geological evolution. Furthermore, although the spatial distribution of some ice-related landform types has been measured and correlated with latitude-controlled climatic processes, broadscale heterogeneity in surface geomorphology exists within latitude bands, suggesting the potential importance of regional geology and climate. Therefore, the spatial distribution of landforms thought to be indicative of ground ice must be assessed in more detail and in a representative way, and the types of materials in which these forms occur must be determined.

A project of strategic, targeted mapping of water- or ice-related surface landforms was therefore undertaken to understand the geological and stratigraphic character of the Martian northern plains, with particular regard to the role that ground ice has played in their evolutionary history. We used a grid mapping approach (e.g., Ramsdale et al., 2017) with the latest middle- to high-resolution images of Mars to study its northern large basins (Arcadia, Acidalia, and Utopia Planitiae). The aims were to compare and to contrast the assemblages of landforms and their latitudinal distribution across these three regions and to attempt to determine the origin of some of these materials (Orgel et al., 2018; Ramsdale et al., 2018). Grid mapping is an efficient method to deal with the problems of mapping small landforms over large areas by providing a consistent and standardized approach to spatial data collection (Ramsdale et al., 2017; Voelker et al., 2017).

Here we describe our geomorphological mapping of western Utopia Planitia (UP) along a 300-km-wide strip from 30°N to 80°N and centered on about 90°E (Figure 1a). The goals were to (i) characterize the morphotypes and patterns of the spatial distribution of the landforms, (ii) identify their association with subtly expressed

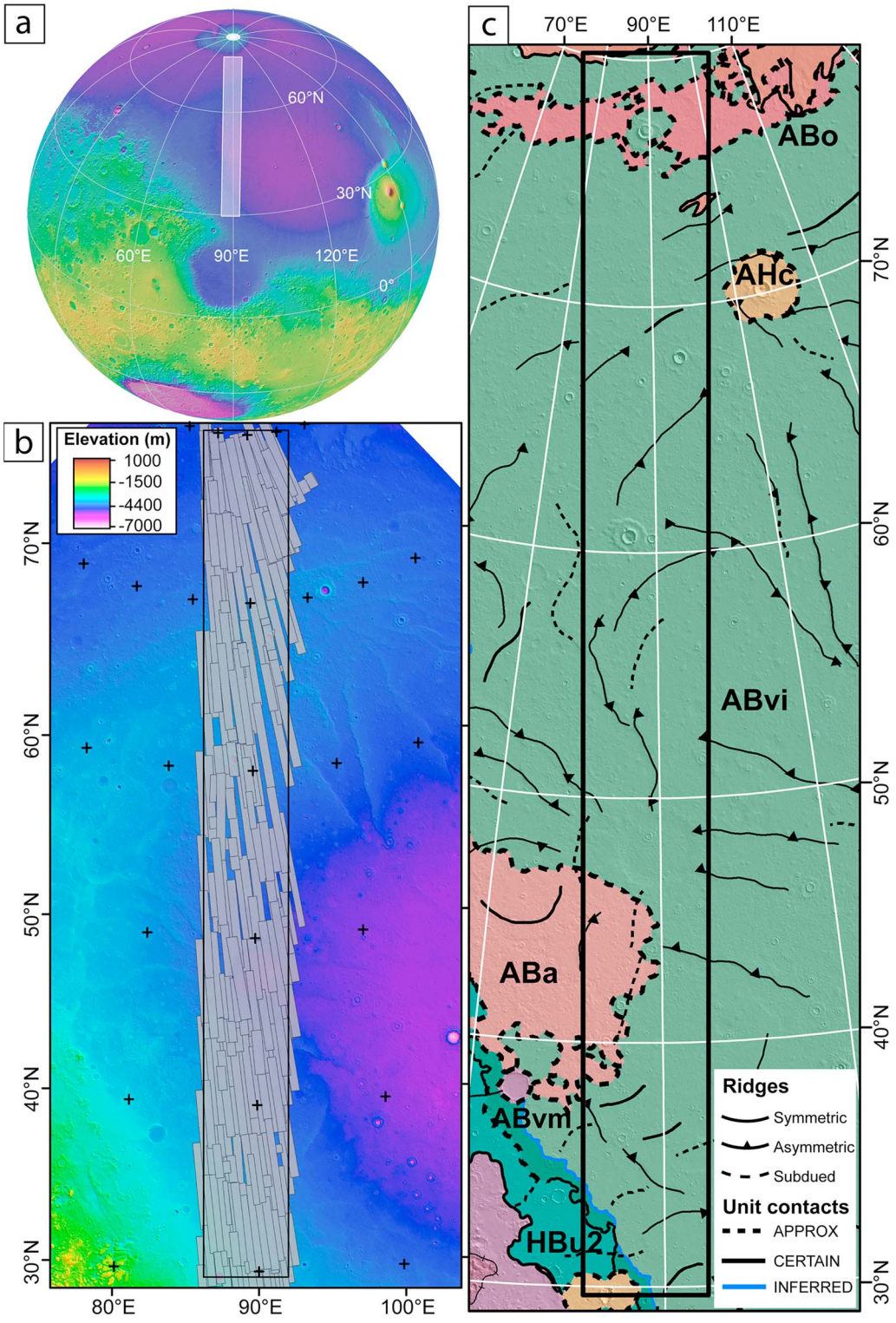


**Figure 1.** Grid mapping in western Utopia Planitia. (a) Localization of the strip in the northern plains (Mars Orbiter Laser Altimeter digital elevation background). (b) Context Camera image footprints used in this study overlaying Mars Orbiter Laser Altimeter map. (c) Study area over the geological map of the northern plains from Tanaka et al. (2005). ABvi = Vastitas Borealis interior unit; ABvm = Vastitas Borealis marginal unit; HBu2 = Utopia Planitia 2 unit; ABa = Astapus Colles unit; ABo = Olympia Undae unit; AHc = Crater unit. See more details in the text.

geological units, and (iii) interpret the cryolithology (ice content, sediment type) of the permafrost and environmental evolution in UP.

## 2. Geological Background of UP

UP centered at ~45°N and ~110°E (Figure 1a) is one of three major topographic basins in the northern hemisphere of Mars (McGill, 1989; Thomson & Head, 2001). The average elevation within the studied zone is about −4,100 m (Figure 1b). The Vastitas Borealis formation (VBF) covers most of UP and is composed of the *Vastitas Borealis interior* unit and the *Vastitas Borealis marginal* unit (Figure 1c; Tanaka et al., 2005). These units are interpreted to be Late Hesperian (~3.5 Ga) outflow channels sediments (Kreslavsky & Head, 2002a; Tanaka et al., 2005; Werner et al., 2011). The Late Hesperian *Utopia Planitia 2* unit in the south was most probably formed by erosion and redeposition of Noachian highland material (Figure 1c; Tanaka et al., 2005). The VBF itself is overlain by the Middle to Late Amazonian *Astapus Colles* unit, which is thought to be an icy mantle emplaced by atmospheric precipitation and possibly predating the LMD (Figure 1c; Skinner et al., 2012; Tanaka et al., 2005). In the north, the Olympia Undae unit is formed by extensive dune fields (Tanaka et al., 2005).

## 3. Data and Method

### 3.1. Grid Mapping

The geomorphological grid mapping was performed along a 300-km-wide strip from 30°N to 80°N (from about 87°E to 93°E at 30°N; Figure 1b). To ensure a high spatial coverage of the study area and a good resolution, Context Camera (CTX) images (6 m per pixel) were used (Figure 1b; Malin et al., 2007). Complementary High Resolution Imaging Science Experiment images (25 cm per pixel; McEwen et al., 2007) helped in the study of some of the landforms. Mars Orbiter Laser Altimeter (MOLA)-gridded global digital elevation data were used for regional topographic analysis (463 m per pixel), whereas detailed local topographic considerations were obtained through MOLA Precision Experiment Data Record laser shots analysis (vertical uncertainty of about ~1 m, horizontal precision ~100 m, with distance between individual shots on average 300 m; Smith et al., 2001, 2003).

The mapping strip was divided into a grid of 15 × 150 squares, each approximately 20 km across (Figure 2). The Cassini projection (centered at 90°E longitude) was chosen to give minimal distortion along the central meridian, ideal for a long and narrow north-south strip. Using ArcGIS software, the grid system was set up as a polygon shapefile, in which each grid square was represented by a single-square polygon object (more details in Ramsdale et al., 2017). Grid mapping is an efficient method to map small landforms over large areas (Ramsdale et al., 2017). Across the region, different water- or ice-related landforms were identified to understand the distribution and role of ground ice in UP (Figure 2). More details are provided in Ramsdale et al. (2017). The landforms were recorded in each grid square with a code as either 1 for "present," 1.5 for "extensive," 2 for "dominant," 0 for "absent," or P for "possible" (Figure 2). The code N means an absence of CTX images. The "dominant" classification was used when a single landform type covered the entire grid square to such an extent that other landforms were obscured. The end result of the mapping was a raster-like data product of the distribution of landforms across the whole strip, hence providing a digital geomorphological map (Figures 2 and S1).

### 3.2. Crater Size-Frequency Distribution Measurements of Small Impact Craters (>50 m in Diameter)

Recently, small impact craters (10- to 100-m scales) and high-resolution images have been used to distinguish climate events of the Late Amazonian despite some uncertainties, such as the role of secondary craters or postimpact modification of crater rim (e.g., Daubar et al., 2013; Hartmann & Daubar, 2017; Hartmann & Werner, 2010).

We measured crater size-frequency distributions (i.e., numbers of craters accumulated on surface units) using CTX images to provide a crater retention age for the different geomorphologic units (e.g., Hartmann & Neukum, 2001; Ivanov, 2001). All visible impact craters (>50 m in diameter) were measured except the aligned secondary clusters and rays within the CTX resolution limit using the CraterTools ArcGIS add-in (Kneissl et al., 2011). Three zones comprising several grid cells were selected in places without extensive degradation and dust deposits following our interpretation of assemblages of landforms (black squares in

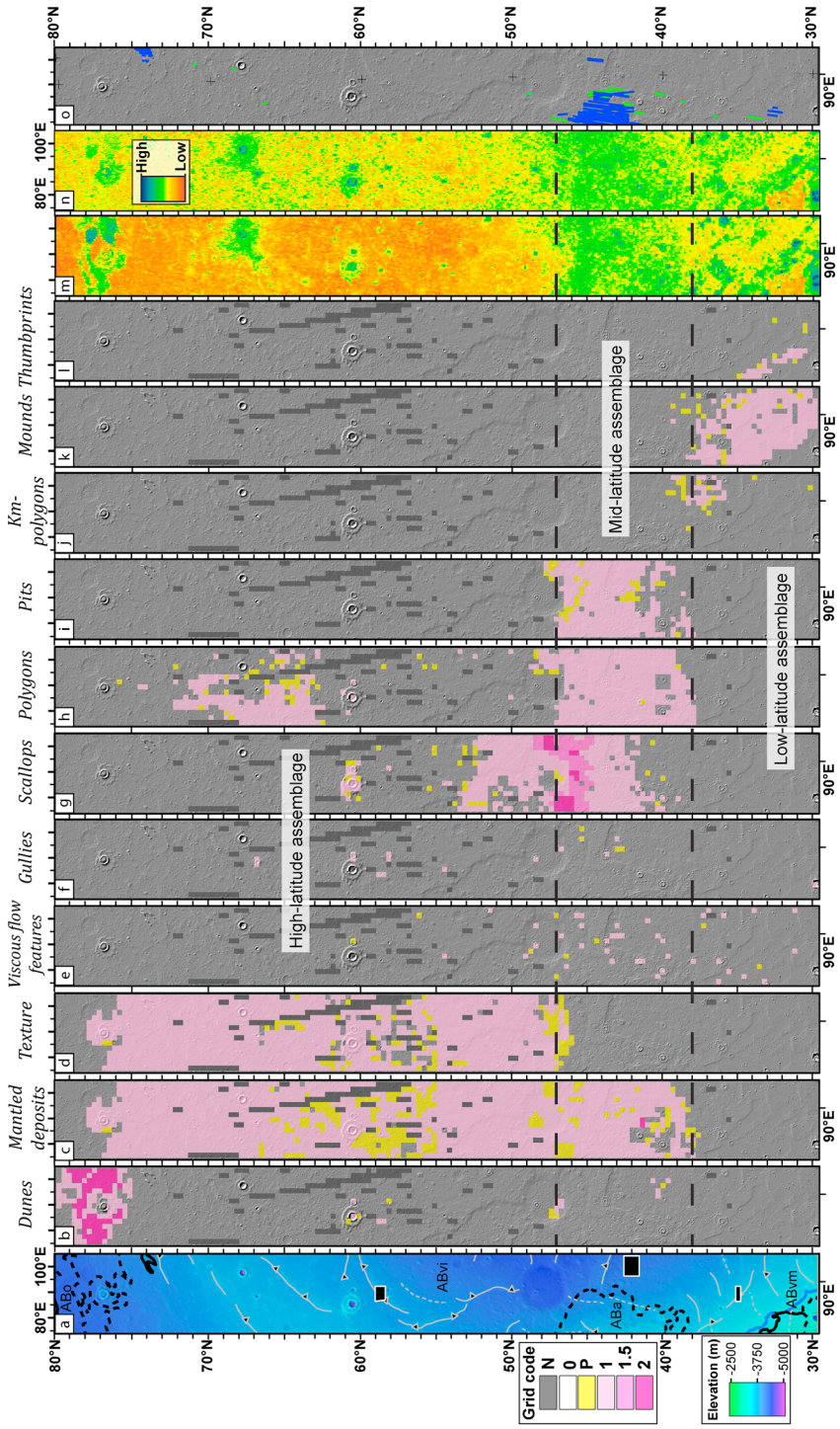


**Figure 2.** Three assemblages of landforms can be distinguished in Utopia Planitia based on their associations at regional and local scale as well as correlation with latitude and topographic roughness at 600-m scale. (a) MOLA topographic map with geological units of Tanaka et al. (2005). See more details in the text and in Figure 1. Crater count areas for geomorphological units (black squares). (b–l) Distribution of landforms within the grid mapping with a MOLA hillshade background. The landforms were recorded in each grid square (20 km across) as either "absent 0," "possible P," "present 1," "extensive 1.5," or "dominant 2." N means an absence of Context Camera images. MOLA topographic surface roughness represented at (m) 600- and (n) 2,400-m scales, modified from Kreslavsky and Head (2000). (o) SHAllow RADar subsurface reflections (blue) and possible reflections (green) associated with ice regolith or regolith basement interfaces. ABvm = Vastitas Borealis marginal unit; ABvi = Vastitas Borealis interior unit; ABa = Astapus Colles unit; ABo = Olympia Undae unit; MOLA = Mars Orbiter Laser Altimeter.

Figures 2a and S3). Counting areas >1,000 km$^2$ were considered, because they have been shown to have lower uncertainties than counting areas <100 km$^2$ (Warner et al., 2015).

Three morphological crater classes were selected to highlight potential multiple resurfacing events following a similar procedure described in Hartmann and Daubar (2017): "fresh," "modified," and completely "filled" craters. Fresh craters were defined as craters with an undegraded rim and bowl-shaped dark interior that does not show any evidence of sublimation (Figure S2a). Modified craters represent craters that have a smoothed rim and shallow interior (no clear bowl shape) due to mass wasting or some infilling (Figure S2b). Modified craters were distinguished from nonimpact pits formed by sublimation by their regular, circular outline, and bowl shape. Filled craters contain deposits completely filling the crater interior up to their irregular and low-relief rim (Figure S2c).

Then we follow a "three-count" procedure. First, only the fresh craters were counted to estimate the date of last disturbance of the surface (i.e., pristine craters postdate the last resurfacing event). Second, for comparison, a second count that included the fresh and modified craters was performed to estimate the total survival time of the oldest, most modified craters that could correspond to another major resurfacing event. Finally, we counted separately the filled craters to give an estimation of the formation age of the buried underlying surface (Platz et al., 2013). This procedure gives insight into the different resurfacing and deposition that may have occurred and brackets a lower and upper temporal limit.

The three crater size-frequency distributions were plotted with Craterstats 2.1 software using a differential plot, similar to the incremental presentation used by Hartmann and Neukum (2001). The difference between the two plotting types is that the differential plot is normalized according to the choice of bin width such that the plot is independent of the binning (aside from statistical effects; Michael, 2013). We chose a 10-per-decade binning to have a compromise between accuracy and smoothing of the data. The crater retention ages were calculated with Craterstats by visually selecting the portion of the crater size-frequency distributions that is parallel to some isochrons between steps of the distribution. The "Mars, Hartmann 2004 iteration" chronology system was used with the "Mars, Michael (2013)" chronology function and the "Mars, Hartmann (2005)" production function (Hartmann, 2005; Michael, 2013).

### 3.3. SHAllow RADar Subsurface Reflections

We analyzed 129 observations from the SHAllow RADar (SHARAD) instrument that cross the UP swath (Figure 2o). The aim was to detect radar reflections that represent an interface between contrasting materials: air regolith, regolith ice, and regolith basement. In this grid mapping survey we searched for detection interfaces and postulated on the materials that were observed. Radar profiles were interpreted in several steps to avoid artifacts and reflections from surface topography (see more details in Smith & Holt, 2015; Figure S4). Material properties are discussed in the supporting information.

## 4. Distribution of Landforms in UP

### 4.1. Mantled Deposits

Mantled deposits were defined as areas that appear subdued by a deposit over several kilometers. An example of this mantling would be filled impact craters (Figure 3a). We emphasize that these deposits do not necessarily correspond to the young LDM as other mantles were identified in multiple northern lowland locations. They are especially noticeable in a form of relief softening over several grid cells (Figure 3b). Mantled deposits are observed at latitudes >38°N up to the polar cap, where in turn they are covered by an extensive dune field around 75°N (Figures 2b and 2c).

### 4.2. Textured Terrains

At high latitude, the surface can have a very distinctive decameter scale texture of evenly spaced knobs, referred to as "basketball terrain" (Figure 3b; Malin & Edgett, 2001). The knobs are made of accumulations of boulders (<1 m) that are locally concentrated in piles (3–5 m) and regularly spaced (20–35 m; Levy, Marchant et al., 2010; Mellon et al., 2008). Rubble piles can be observed on top of smaller polygons (6–25 m in diameter). Formation mechanisms are unclear but may involve gravitational sorting of boulders into polygon troughs and differential sublimation (Levy et al., 2009a; Mellon et al., 2008). Textured terrains are present from ~47°N up to 78°N, where it is covered by an extensive dune field (Figure 2d).

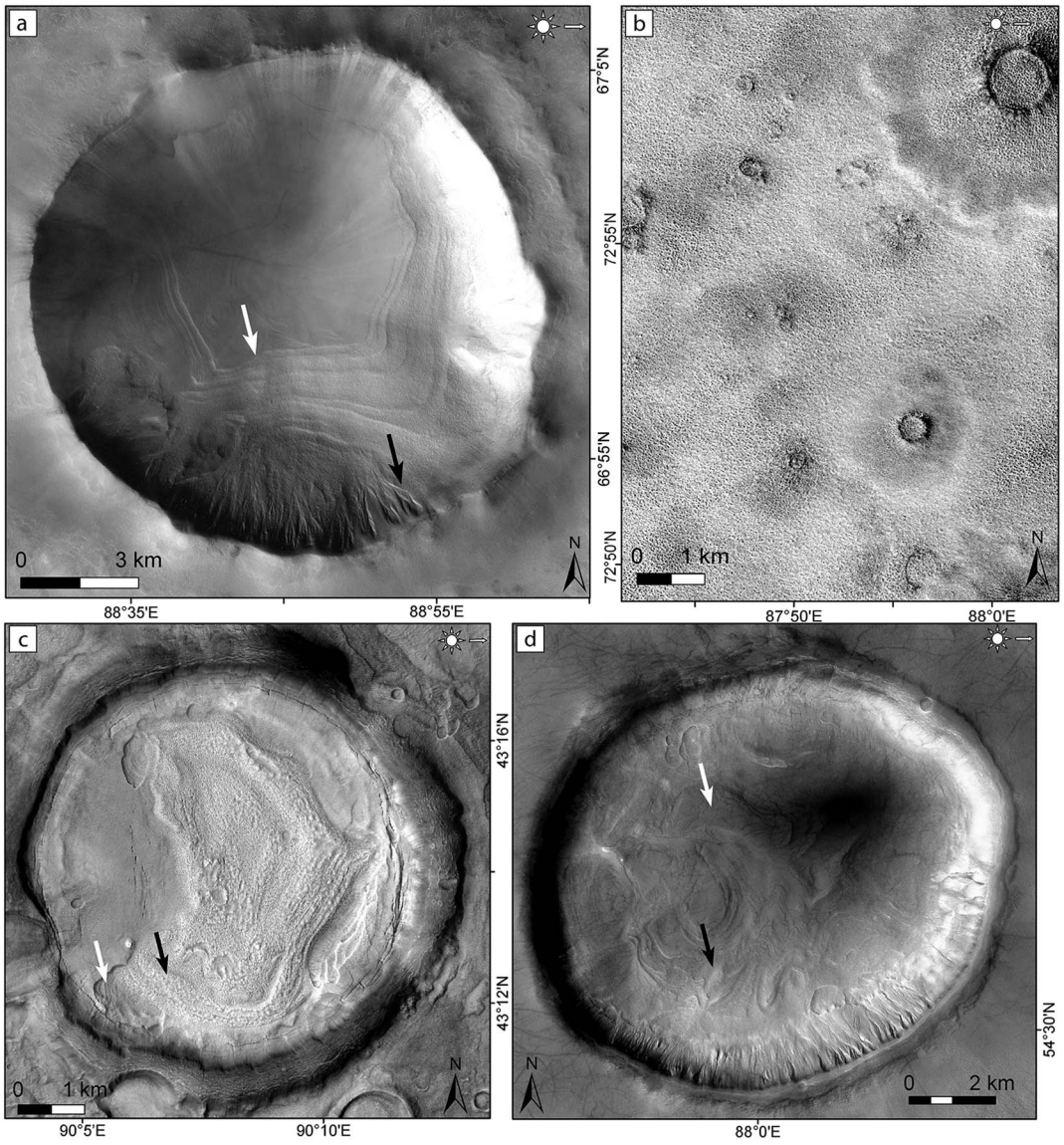


**Figure 3.** Ice-related landforms smoothing the topography. (a) Mantled deposits with layers (white arrow) covering the interior of an impact crater. Gullies occur on the north-facing slopes eroding the mantled deposits (black arrow). Context Camera F02_036670_2450_XN_65N270W. (b) The basketball terrain type consists of evenly spaced knobs that are ubiquitous over the smoothed relief of mantled deposits. G01_018763 2538_XN_73N273W. (c) "Classic" CCF with the typical brain terrain texture, concentric deformation (black arrow), and local degradation by scallops (white arrow). B17_016126_2348_XN_54N272W. (b) "Low-definition" CCF instead have a muted, undulated surface texture at broadscale (black arrow). Smooth latitude-dependent mantle overlies some portion of CCF surfaces (white arrow). P13_006184_2233_XN_43N269W. CCF = concentric crater fills

### 4.3. VFF

VFF are interpreted as debris-covered/rock glaciers deformed by downslope flow, forming lineations (e.g., Carr, 2001; Head et al., 2010; Souness et al., 2012; Squyres, 1979). Different morphological types are recognized: lineated valley fill, lobate debris aprons, concentric crater fills (CCF), and glacier-like forms. In the study area, the VFF occur only as CCF inside impact craters larger than 3 km in diameter and at latitudes of 30°–55°N (Figure 2e).

In UP, two morphological subtypes of CCF were defined: "classic" and "low-definition" (Levy et al., 2010). The classic CCF are crater-interior units showing multiple concentric lineations formed by downslope flow in some part and typically display a "brain terrain" surface texture (Figure 3c). The brain terrain texture is

interpreted to be due to differential sublimation through fractures in the debris-covered massive ice (Levy et al., 2009b; Mangold, 2003). According to our mapping, these classic CCF occur between 30°N and about 47°N (Figure 2e). The low-definition CCF have a muted undulated surface texture at broadscale (Figure 3d; Levy, Head et al., 2010). Smooth younger LDM overlies some portion of the CCF surface and has little evidence of deformation associated with CCF flow (Levy et al., 2009b). For latitudes >45°N, the brain terrain is progressively overlapped by this deposit until more or less complete burial at latitudes >48°N (Figure 2e).

### 4.4. Gullies

Gullies are composed of an alcove feeding into a channel, terminating with a depositional apron (Figure 3a; Malin & Edgett, 2000). They may indicate recent liquid water (e.g., Malin et al., 2006), supplied by the melting of snow packs (Christensen, 2003) or near-surface ground ice (Costard et al., 2002), or they could result from "dry" mass movement processes (e.g., Pelletier et al., 2008; Treiman, 2003) related to seasonal $CO_2$ frost (Cedillo-Flores et al., 2011; Musselwhite et al., 2001).

In the studied area, the gullies are present from about 30°N to 67°N (Figure 2f). All identified gullies in this region are present on the inner walls of 10 large impact craters (>8 km in diameter; Figure 3a). Gullies are mostly present on the north-facing inner slopes (in 7 out of 10 craters) and the west-facing inner slopes of craters (in 6 out of 10 craters).

### 4.5. Scalloped Depressions

Scalloped depressions in UP have circular to elliptical shapes with diameters ranging from tens of meters to several kilometers and depths up to several tens of meters (Figure 4; Costard & Kargel, 1995; Lefort et al., 2009; Morgenstern et al., 2007; Séjourné et al., 2011; Soare et al., 2005, 2007, 2008; Ulrich et al., 2010). They are characterized by an N-S asymmetric profile showing curvilinear steps; their pole-facing slopes are steeper (5°–20°) than their equator-facing slopes (2°–5°; Lefort et al., 2009; Morgenstern et al., 2007; Séjourné et al., 2011). The scallops have been proposed to be the result of ground ice melting (Costard & Kargel, 1995; Soare et al., 2005, 2007, 2011) or sublimation of ground ice (Lefort et al., 2009; Morgenstern et al., 2007; Séjourné et al., 2011; Ulrich et al., 2010; Zanetti et al., 2010). The scalloped depressions therefore form by removal of excess ice (i.e., the amount of ice exceeding the natural pore water content in a nonfrozen state) followed by collapse of the ground. Thermokarst denotes the processes and landforms associated with the volumetrically substantial loss of excess ice and resulting subsidence (French, 2007; Van Everdingen, 1998). In the paper, we will refer to "thermokarst" as degradation of excess ice either by melting or sublimation following French (2007).

The scalloped depressions are observed over the latitudes from ~38°N to 61°N (Figure 2g). Four distinct zones can be distinguished based on differences in the diameter, shape, and concentration of scallops. Between the four zones, the change in morphology and concentration of scallops is relatively abrupt and is not associated with a difference in elevation or geological units (Figure 2g).

(1) A local occurrence of scallops around 58°–60°N is only observed on pedestal and lobate ejecta craters. We observed small- to medium-sized depressions with a diameter ranging from 0.1–5 km (Figure 4a). (2) A northern zone from ~47°N to 54°N, where small-sized shallow scallops (0.1–1 km in diameter) cover the plains and crater interiors (CCF; Figure 4b). For latitudes >53°N, the size and number of scallops decrease sharply northward (Figure 2g). (3) A central zone between ~45°N and 47°N, where numerous coalesced, nested, medium-sized depressions (1–5 km in diameter) and large-sized deep scallops (20–50 km in diameter) are observed in high concentration (Figure 4c). In the grid mapping, medium-sized depressions are coded as "1.5," while large-sized ones are coded as "2" (Figure 2g). We did not observe any depressions around 48°N/90°E because of extensive sand and dust deposits (Figure 2g). (4) A southern zone from ~40°N to 45°N, where small- and medium-sized isolated scallops (0.5–5 km in diameter) are scattered on the plains (Figure 4d). Many depressions are observed around the exhumed ejecta of large impact craters (1–10 km in diameter). The number of scallops decreases southward down to 40°N. For latitudes <43°N, the ejecta of large impact craters with diameters larger than 3 km are completely exhumed while the crater interior is still partially filled.

### 4.6. Small-Sized Polygons

Different small-sized polygonal patterned ground with morphology and scale consistent with thermal contraction cracking of permafrost occur in UP (Lefort et al., 2009; Mangold, 2005; Morgenstern et al., 2007;

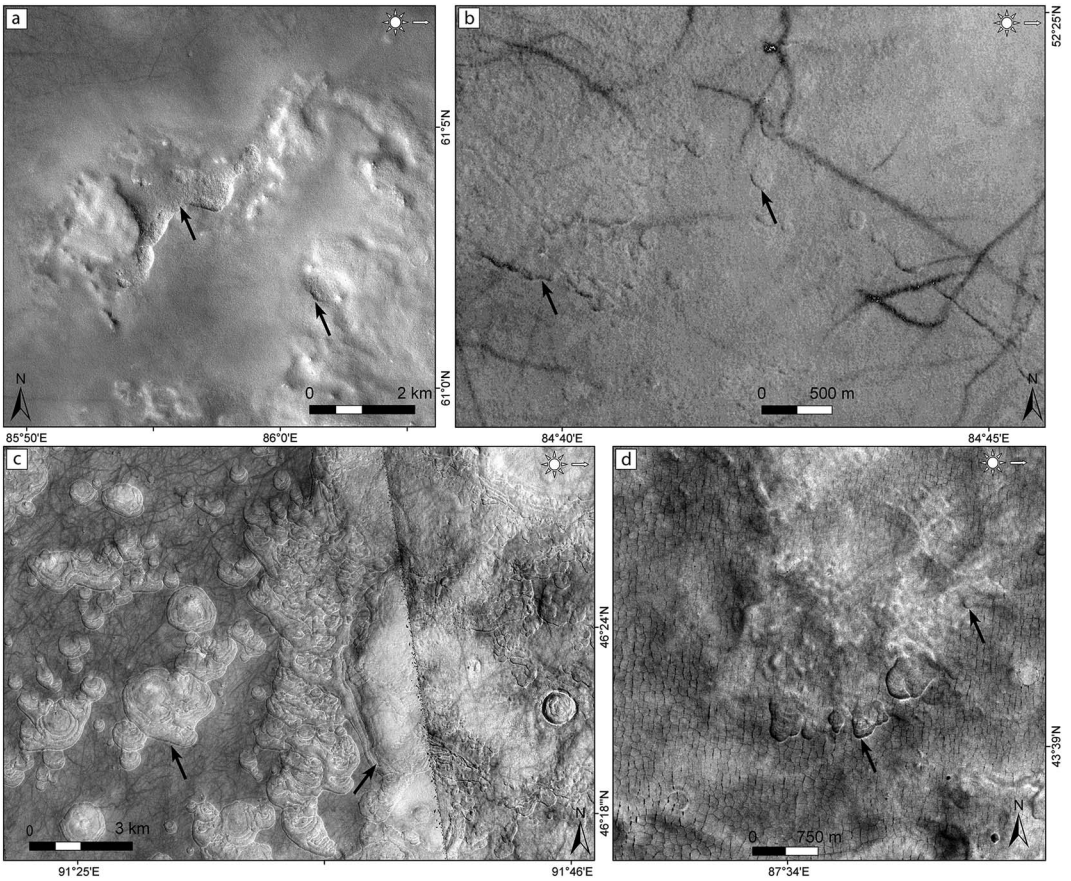


**Figure 4.** Four zones are distinguished based on the morphologies and the concentration of scalloped depressions. (a) Medium-sized (0.1–5 km in diameter, coded as 1 in the grid) scallops (black arrow) on ejecta of a lobate craters. Context Camera B01_010179_2408_XN_60N274W. (b) A northern zone with small-sized (0.1–1 km in diameter, coded as 1) shallow scallops (black arrow). G23_027163_2305_XN_50N274W. (c) A central zone with numerous medium-sized scallops (1–5 km in diameter, coded as 1.5 in the grid) and large-sized deep ones (20–50 km in diameter, coded as 2). P19_008478_2246_XI_44N268W. (d) A southern zone with scattered medium-sized (0.5–5 km in diameter, coded as 1 in the grid) single scallops (black arrow) that are scattered on the plains $<$43°N. B18_016759_2236_XN43N272W.

Seibert & Kargel, 2001; Séjourné et al., 2011; Ulrich et al., 2010). According to our mapping, two types of polygons are present in two distinct zones (Figure 2h). At high latitudes between ~53°N and 75°N, the polygons have a rectangular to hexagonal shape and are ~20–50 m in diameter (Figure 5a). They occur both on the smooth relief of the plains and on buried impact craters. We observed that in some places, the polygons were better identified when frost deposited along the troughs underlines the network on CTX images (left side of the Figure 5a). Therefore, their distribution may be more extensive than currently mapped.

At midlatitudes between ~38°N and 50°N, the polygons are rectangular with a larger typical diameter of about 100 m (Figures 2h and 5b). Over this area, these polygons form a continuous polygonized surface on the intercrater plains with a regular N-S orientation. In areas with significant local relief (e.g., ridge or hill), the network of polygons shows a particular orientation, parallel or orthogonal to the local slope (black arrow on Figure 5b; French, 2007). The southern limit of their distribution (about 38°N) is very sharp (Figure 2h). The northern limit (around 48°N) is uncertain and corresponds to areas where the polygons are progressively totally degraded by scallops and covered by sand deposits.

### 4.7. Polygon-Junction Pits

The rectangular polygons of 100 m in diameter show pits exclusively along their N-S troughs (referred to as polygon-junction pits; black arrow on Figure 5b; Seibert & Kargel, 2001). The pits are elongated to

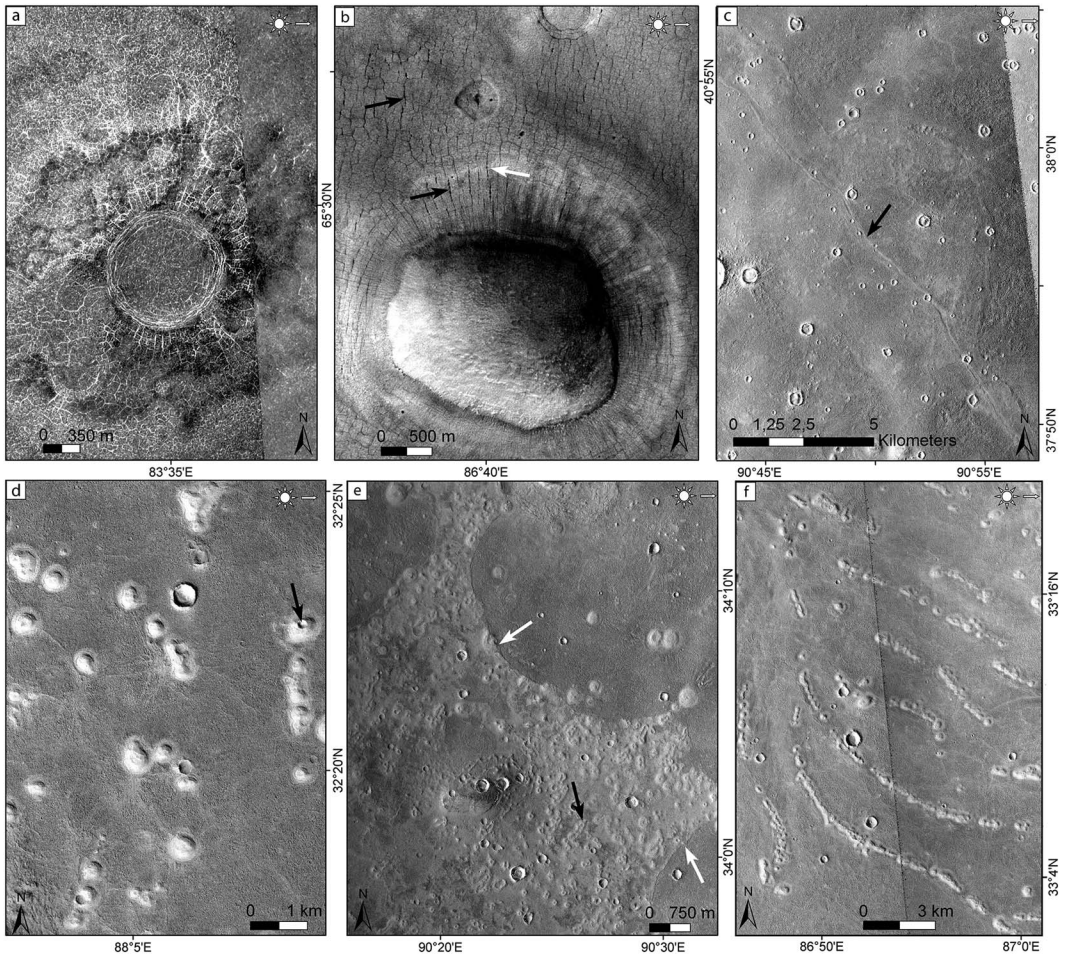


**Figure 5.** Polygons and mounds in Utopia Planitia. (a) High-latitude polygons of 20–50 m in diameter occur on the plains and on filled impact craters. Context Camera D18_034112_2459_XI_65N275W/D17_033967_2459_XI_65N277W. (b) Midlatitude rectangular polygons of 100 m in diameter have an N-S elongation. In areas of local relief, the long axis of polygons is oriented along the local slope (white arrow). Semicircular pits (black arrow) are only located along the troughs of these polygons. P16_007384_2216_XN_41N273W. (c) Kilometer-scale polygons are only observed in a form of wavy shallow troughs of 10–20 km in length (black arrows). F01_036235_2161_XN _36N269W. (d) High-albedo mounds composed of large pitted domes (500 m in diameter; black arrow) and smaller mounds (50–300 m in diameter) generally concentrated in large fields. They can be coalesced and aligned along an SW-NE direction (black arrow). Lobate deposits (white arrow) locally overlap some mounds. P12_005815_2128_XI_32N272W and B17_016126_2126_XI_32N269W. (e) Thumbprint terrains form parallel and curvilinear ridges composed of aligned coalesced mounds or chains of individual ones. The curvilinear ridges range from 1 to 5 km in length with a convex shape indicating a general SW direction. B05_011656_2137_XI_33N273W.

circular with a diameter ranging from 10 to 150 m for a depth of 5–40 m (Costard et al., 2016; Morgenstern et al., 2007; Soare et al., 2011). They were interpreted to be due to thermokarst degradation of the troughs either by sublimation, or surface or underground melting of ground ice (Costard et al., 2016; Morgenstern et al., 2007). They often crosscut or incise the scalloped depressions suggesting a concomitant or subsequent formation (Lefort et al., 2009). The pit distribution and the polygon distribution overlap (38°–47°N; Figure 2i).

### 4.8. Kilometer-Scale Polygons

In southern UP, polygons of 5–20 km in diameter are irregularly shaped and occasionally not completely closed (Buczkowski et al., 2012; Hiesinger & Head, 2000; Pechmann, 1980). They may have been formed by desiccation or compaction of previously water-rich sediments (Buczkowski & McGill, 2002; Pechmann, 1980), possibly in combination with an elastic rebound after removing water or ice from the ground

(Hiesinger & Head, 2000). They occur between 36°N and 40°N (Figure 2j). We observed only wavy shallow troughs of 100–200 m in width and 10–20 km in length (Figure 5c).

### 4.9. High-Albedo Mounds

In the northern plains, several circular cones or mounds have been studied. They are usually interpreted to be rootless cones or cinder cones (Frey & Jarosewich, 1982; Plescia, 1990), pingos (Burr et al., 2009; Soare et al., 2005), or mud volcanoes (Farrand et al., 2005; Ivanov et al., 2014; McGowan, 2011; Skinner & Mazzini, 2009). The mounds are high-albedo features with a domed top and sometimes a central pit (Figure 5d). Large mounds (500 m in diameter) are scattered over the plain, while smaller mounds (50–300 m in diameter) are generally grouped in large fields (Figure 5e). In some places, lobate deposits of several kilometers in length overlap the mounds (white arrow on Figure 5e). Interestingly, some small mounds can be coalesced forming a ridge along an SW-NE direction (black arrow on Figure 5e). They are present between 30°N and 40°N with a higher concentration for a 30°–35°N band (Figure 2k).

### 4.10. Thumbprint Terrains

Thumbprint terrains consist of sets of parallel curvilinear ridges or pitted cone chains, with individual segments up to several tens of kilometers in length (Figure 5f; Kargel et al., 1995). These features occur in various locations on the northern plains. Based on their morphology and analogy with Earth, they have been interpreted as mudflows (Jöns, 1986) or mud volcanoes (Farrand et al., 2005; McGowan, 2011). Recently, thumbprint terrains near Arabia Terra were observed in association with runup lobate deposits and interpreted as tsunami deposits (Costard et al., 2017; Rodriguez et al., 2016). In UP, the thumbprint terrains are present from 30°N to 40°N within a narrow zone oriented in an NW-SE direction (Figure 2l). The curvilinear ridges range from 1 to 5 km in length with a general convex shape toward the SW (Figure 5f). The mounds forming the ridges have a dome-like shape of several hundred of meters in diameter with a central pit.

## 5. Interpretation

### 5.1. Three Assemblages of Landforms in UP

Assemblages of landforms can be defined based on the spatial association at regional and local scale of landforms and their formation under similar climatic and geomorphologic conditions, hence constituting a coherent landscape. The range of occurrence of the landforms can highlight trends in their distribution and potential association. The distribution of landforms is correlated with latitude and MOLA roughness at 600-m scale but less with elevation (Figures 2a, 2m, and 2n). Based on these relationships, three assemblages of landforms can be distinguished.

The high-latitude assemblage is composed of mantled deposits, textured terrains, and ~20- to 50-m-diameter polygons that are correlated between ~47°N and 78°N (Figure 2). The surface of the mantled deposits is textured at local scale (Figures 2c, 2d, and 3b). The mantled deposits show also polygons between 61°N and 75°N. The occurrence of this landform assemblage (47°–78°N) is correlated with a low MOLA topographic roughness at 600- and 2,400-m scales (smoothing of topography; Figures 2m and 2n). The subkilometer smoothing, extending to the northern hemisphere, of topography indicates the presence of the young LDM (Head et al., 2003; Mustard et al., 2001). From the observation of polygons and textured terrains, the LDM underwent thermal contraction, cryoturbation, and differential sublimation of the upper meter (Head et al., 2003; Kreslavsky & Head, 2002b; Mellon et al., 2008). From 47°N to 61°N, the surface shows numerous small-sized scallops (Figure 2g). The LDM is thought to be degraded in the midlatitude zones (30°–60° and referred to as a dissected mantle), whereas at high latitudes $>60°$, the mantle is intact (referred to as a continuous mantle; Mustard et al., 2001).

The midlatitude assemblage comprises scallops, 100-m-diameter polygons, pits, and mantled deposits that are correlated in a zone between ~38°N to 47°N (Figure 2). They are spatially associated at small scale, where the polygons occur on the mantled deposits. The polygons are degraded by the scallops and by the pits (Figure 4d). Their spatial association indicates an assemblage of landforms (Morgenstern et al., 2007; Soare et al., 2007, 2011). By analogy with ice-rich permafrost landscapes on Earth that have a similar assemblage of landforms (thermokarst lake and thermal contraction polygons), this zone is interpreted to be a degraded ice-rich permafrost (Lefort et al., 2009; Morgenstern et al., 2007; Séjourné et al., 2011; Soare et al., 2007). The association of these landforms was previously shown

at local scale but not at regional scale. According to Kreslavsky and Head (2000), this zone in UP has a higher MOLA roughness at 600- and 2,400-m scales than other places in the northern plains (Figures 2g, 2m, and 2n). The strong correlation with the 600-m-scale roughness is due to the presence of numerous depressions of 250–1,000 m in diameter, with a higher roughness being observed in the central zone (45°–47°N) due to a higher number of nested depressions (Figure 4c). The correlation with the 2,400-m-scale roughness is due to the presence of kilometric depressions (also higher number for the central zone) and exhumed impact crater with ejecta.

The low-latitude assemblage is composed of kilometer-scale polygons, high-albedo mounds, and thumbprint terrains that occur mostly between ~30°N and 38°N (Figure 2). Their close spatial association and the similarity in their morphological characteristics point to an assemblage of landforms. This assemblage occurs at an elevation between −3,600 and −4,000 m. Its distribution is correlated with a medium MOLA roughness at 600- and 2,400-m scales (Figures 2m and 2n). Collectively this assemblage of landforms was interpreted as mud flows from diapirism or compaction (Buczkowski et al., 2012; Ivanov et al., 2014; McGowan, 2011; Skinner & Mazzini, 2009).

Gullies and concentric crater fills have a broader distribution and do not seem to be correlated with any assemblage of landforms in particular (Figure 2). The gullies are not observed above 67°N. In the northern plains, a decrease in gully frequency for latitudes >45°N is correlated with the poleward decline of the topographic roughness at 600-m scale and consequence lack of steep slopes (Figure 2f; Dickson & Head, 2009). Therefore, the absence of gullies may be caused by lack of appropriate craters with steep enough slopes. The CCF are no observed at high latitudes because they are progressively overlapped by the LDM until more or less complete burial at latitudes >47°N (Figure 2e).

### 5.2. Geomorphological Units

We identified two deposits that are associated with the low- and middle-latitude assemblages of landforms forming geomorphological units. The southwestern limit of the low-latitude assemblage of landforms is correlated with several lobate deposits (Figure 6a). This limit corresponds to the southern limit of the Vastitas Borealis interior unit (Figure 2a; Ivanov et al., 2014; Jöns, 1986; Kargel et al., 1995; Tanaka et al., 2005). This landform assemblage is thus correlated with this deposit, which covers the southeastern portion of the study area. Based on MOLA laser tracks, the thickness of the lobes was estimated to be 20–30 m (Figure 6b). The lobes each have a ridge at the front (white arrow on Figure 6b). These lobes share similar morphologic characteristics with the runup lobate deposits that were recently interpreted as tsunami deposits (Costard et al., 2017; Rodriguez et al., 2016). All of these features superimpose the VBF and collectively suggest that there was a large (1,000-km diameter) reservoir of water/mud in the deepest portions of the Utopia basin (Ivanov et al., 2014; Skinner & Mazzini, 2009).

The southern limit of the midlatitude assemblage of landforms takes the form of a polygonized deposit with clearly defined, gently sloping limits (Figure 6c). In some places, the deposit partially covers hills (dashed lines on Figure 6c, compare with the hill on Figure 5b). The deposit covers a surface that is lower in altitude (gray symbols) and partially buries some impact craters (black arrow). This underlying rough surface contains large high-albedo mounds of the previously mentioned assemblage of landforms (white arrow). The estimated thickness of the deposit is about 40–80 m, based on several MOLA laser tracks along the limit (Figure 6d). The 100-m polygons occur on the front slope of the deposit (Figure 6c). Locally, at higher latitude (around 41°N), similar hills and an underlying rough surface were observed from the degradation of the polygonized surface by scallops (Morgenstern et al., 2007; Soare et al., 2012, 2013). Therefore, we suggest that the midlatitude landform assemblage is correlated with this deposit that covers the low-latitude assemblage. This deposit was not recognized in previous geological maps (e.g., Tanaka et al., 2005, 2014). It is important to note that the scallops are absent along the limit of the deposit, indicating a nondegraded boundary. Additionally, the remarkable continuous morphology of the 100-m polygons over the surface indicates that they necessarily formed after the deposition of the sediment. For example, in places of local relief (ridge or hill), the network of polygons follows the local slope (Figure 5b).

In summary, a geomorphological unit is composed of the midlatitude assemblage associated with a deposit of 80 m in thickness. This unit overlaps another geomorphological unit composed of the low-latitude assemblage associated with a lobate deposit of 30 m in thickness.

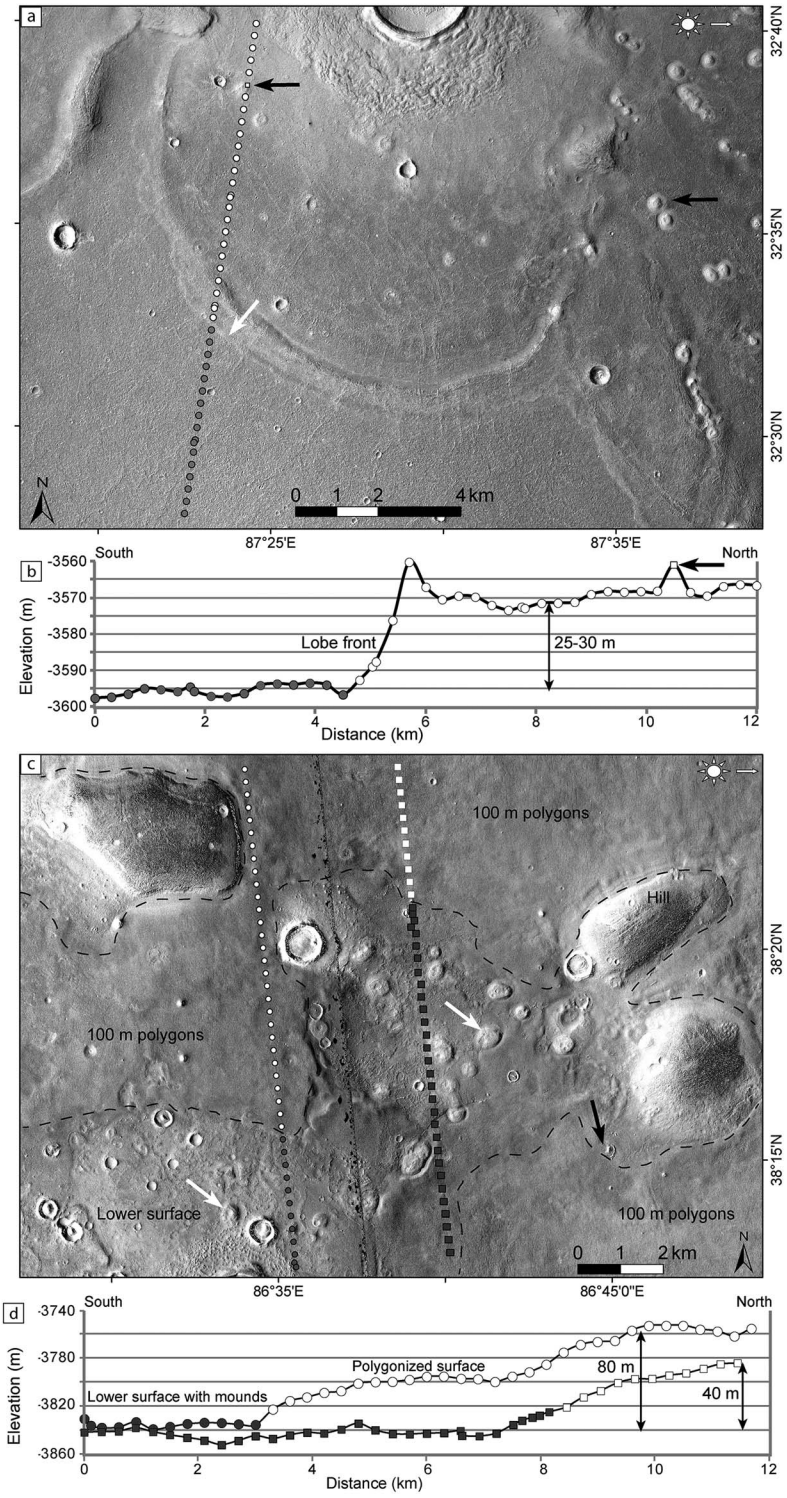


**Figure 6.** Deposits associated with the low- and middle-latitude assemblages of landforms. (a) Lobate deposit associated with the low-latitude assemblage. Large high-albedo pitted (black arrows) occur on the lobate deposit. The deposit has a ridge at the front (white arrow). (b) The thickness of the deposit is about 25 m (white circles). The height of one mound is estimated to be about 10 m (black arrow). Data from Mars Orbiter Laser Altimeter laser shots. Context Camera D18_034099_2111_XI_31N272W. (c) Deposit associated with the midlatitude assemblage. The deposit that has 100-m polygons (dashed lines), partially covers some hills, high-albedo mounds (white arrow), and impact craters (black arrow). (d) The deposit (white symbols) is 40 and 80 m in thickness along the two shot tracks shown. Data from Mars Orbiter Laser Altimeter laser shots. Context Camera D21_035378_2184_XN_38N273.

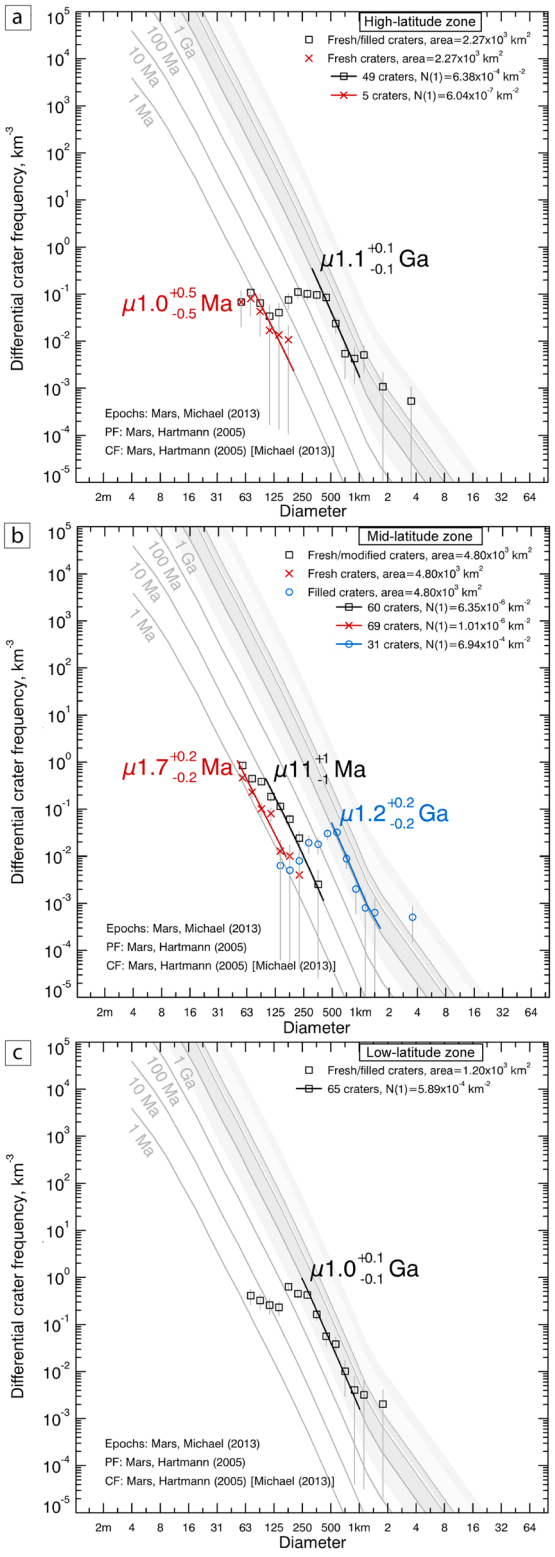


**Figure 7.** Crater size-frequency distributions of the three assemblages of landforms. (a) The high-latitude assemblage where textured terrains occur at 58°N. (b) The midlatitude assemblage where a continuous and undegraded 100-m polygonized surface is present at 42°N. (c) The low-latitude assemblage where high-albedo mounds occur at 35°N. CF = chronology function; PF = production function.

### 5.3. Crater Size-Frequency Distribution Measurements of the Different Geomorphological Units

We measured crater size-frequency distributions (>50 m in diameter) in the zone of the three landform assemblages at 35°N, 42°N, and 58°N (black squares on Figure 2a). For the high-latitude assemblage, fresh and filled craters were counted (Figure 7a). No modified craters were observed. We observe several steps in the crater size-frequency distribution of the complete crater count (black squares). Craters between ~320 m and 1 km, all of which are filled, give a best fit age of 1.1 ± 0.1 Ga. All craters <316 m (bin edge) were partially erased by resurfacing processes after 1 Ga. The fresh and filled craters with diameters between 63 and 126 m (bin edges) are aligned along the 1-Ma isochron. Fresh craters that postdate the last deposition show a similar tendency at diameters between 79 and 160 m (bin edges), with a best fit age of 1.0 ± 0.5 Ma (red crosses; Figure 7a).

For the midlatitude assemblages, filled, modified, and fresh craters were counted on the 100-m polygonized surface (Figure 7b). The distribution of filled craters for diameter >500 m is aligned along the 1-Ga isochron with a best fit age of 1.2 ± 0.2 Ga (blue circles). The count of fresh and modified craters shows a step between the 1- and 10-Ma isochrons (black squares). The craters with diameters >100 m are aligned along the 10-Ma isochron and give a best fit age of 11 ± 1 Ma. They correspond to the last major deposition in the zone. For craters smaller than 79 m (bin edge), a resurfacing event occurred after 11 Ma, partially removing them. The fresh crater distribution fits the 1-Ma isochron with a best fit age of 1.7 ± 0.2 Ma (red crosses; Figure 7b). Given the morphology (shallow interior and smoothed rim) of modified craters (Figure S2), this resurfacing event between 11 and 1.7 Ma could be due to partial filling and/or modification by sublimation of the smallest craters.

For the low-latitude assemblage, filled and fresh craters were counted together for the crater count (Figure 7c). No modified craters were observed. The craters between 250 m and 1 km are aligned along the 1-Ga isochron with a best fit age of 1.0 ± 0.1 Ga (black squares). The crater size-frequency distribution has a step for craters <251 m (bin edge) suggesting that a resurfacing event after 1 Ga partially removed them. Almost all craters appear to be partially filled in the area, so deposition of some material has clearly occurred since 1 Ga (Figure 5c).

In summary, the three crater counts of the three zones provide insight into the different resurfacing and deposition events that have occurred in UP. Using small craters and relatively small areas for dating leads to some uncertainties (e.g., Hartmann, 2005; Hartmann & Werner, 2010), but this method allows the relative comparison of the two crater retention ages. According to the filled crater counts over the three zones, we deduce a best minimum model age for the older cratered basement at ~1.1 Ga. Over the midlatitudes, between 1.1 Ga and 11 Ma, the relative lack of filled craters <500 m in diameter can be explained by the deposition of a layer of about 70–100 m in thickness, assuming depth-to-diameter ratios of about 1:5 to 1:7 for simple bowl-shaped primary crater (Pike, 1977). This interpretation is consistent with our previous estimation of the thickness (Figure 6c) and distribution of mantled deposits over these midlatitudes (Figure 2c).

The fresh craters that postdate the last major resurfacing event give a similar crater retention ages (about ~1.5 Ma) at middle and high latitudes. This

age of the high-latitude landform assemblage corresponds to the time period of LDM deposition (0.4–2.1 Ma; Head et al., 2003; Levy, Head et al., 2010; Mustard et al., 2001; Schon et al., 2012). This age is also in agreement with the age of nondeformed LDM covering the low-definition CCF type (Figure 3d) for latitudes >48°N (~1.5 Ma; Levy et al., 2009b). However, no noticeable difference in topography or clear examples of overlapping deposits are observed around 48°N. At the midlatitudes, the resurfacing event at ~1.7 Ma may be related to deposition a thinner LDM or modification by sublimation. The deposition of a thinner LDM at midlatitudes in UP is consistent with the observation of nondeformed LDM progressively overlapping the older CCF for latitudes >45°N.

### 5.4. Ground Ice Content and Distribution in UP: A Particularly Ice-Rich Area Between 38°N and 47°N

Analysis of the distribution and morphotypes of ice-related features is useful to understand the cryolithology of the permafrost and its past evolution in relation to climate. The middle- and high-latitude assemblages of landforms between 38°N and 78°N are indicative of ground ice and its degradation, but the estimation of ice content is challenging. For example, the midlatitude 100-m polygons are interpreted to have been formed into an ice-cemented permafrost with variable ice content (Levy et al., 2009a; Séjourné et al., 2011; Soare et al., 2011; Ulrich et al., 2010, 2011). Instead of focusing on polygons that have the same morphology from plan view, we suggest that thermokarst landforms such as scallops can be used to get an estimation of the amount of excess ice, although they represent a degradational feature that can be challenging to interpret.

In our previous work, we classified the depressions from small-sized to large-sized scallops to highlight their morphological development with increasing sublimation of ground ice (Séjourné et al., 2011). Based on these considerations and changes in the morphology of the scallops in the midlatitude assemblage (Figure 4), we can classify the thermokarst in the three zones. (1) For latitudes between ~47°N and 54°N, the occurrence of small-sized shallow scallops indicates that the thermokarst has been of relatively low intensity and shallow. (2) For latitudes between ~45°N and 47°N, the presence of numerous large and medium-sized, deep, coalesced scallops and a higher number of polygon-junction pits indicates that the thermokarst has been significant and deep. (3) For latitudes between ~38°N and 45°N and locally on crater ejecta at 58°–60°N, the observation of isolated medium-sized scallops and polygon-junction pits indicates that the thermokarst has been moderate.

On Earth, the morphology and distribution of thermokarst landforms depend on two main factors: thermal destabilization (cause and duration) and cryolithology (amount, structure, and spatial distribution of ground ice; e.g., Jorgenson et al., 2010; Rampton, 1974). Permafrost degradation is always initiated by deepening of the active layer because of an increase in subsurface temperature (French, 2007; Soloviev, 1973). Regional causes include a long-term increase in air temperature and/or precipitation, whereas local causes encompass runoff or ponding of water, local erosion, forest fire, and/or human interaction with the environment. The ice content can vary depending on the type of ice (pore, segregated, or massive ice) and the sedimentary characteristics of permafrost (granulometry, origin; e.g., French & Shur, 2010). Therefore, based on this comparison with Earth, we suggest that the distribution and variation of thermokarst in UP indicate a difference either in (1) sublimation or (2) ice content of the permafrost in UP.

In UP, our first hypothesis proposes that the more severe thermokarst between ~38°N and 47°N than in other areas is due to a higher sublimation of ground ice. This hypothesis is supported by the observation that the boundaries between the three thermokarst areas seem to be controlled by latitude rather than geological units or elevation; therefore, a climatic control is likely. At regional scale, sublimation can be initiated by an increase in surface temperature or a decrease in air humidity (Chevrier et al., 2008; Law & Van Dijk, 1994; Mangold, 2011). Models at this scale show that ground ice in UP is currently stable at depths <0.1 m for latitudes >60°–65°N and unstable at depths >1 m for latitudes <50°–55°N (Chamberlain & Boynton, 2007; Mellon et al., 2004). The distribution of thermokarst corresponds to the latitudes of current instability of ground ice. It does not necessarily mean that the thermokarst was formed during the current obliquity period on Mars but that the ice degradation is consistent with current conditions. With increasing obliquity, the stability of ground ice shifts toward the equator (Chamberlain & Boynton, 2007; Mellon & Jakosky, 1995). From these models, the sublimation of ground ice should be more extensive equatorward. However, this trend is the opposite of the observed decrease in size and number of scallops for latitudes <45°N (Figure 4d). At local scale, sublimation may also

depend on surface properties (e.g., surface albedo) and climatic parameters such as the insolation (surface temperature increase) or wind speed (i.e., decrease in air humidity) or removal of an insulating layer (Van Dijk & Law, 1995). The development of scallops is thought to have been controlled by insolation (Lefort et al., 2009; Morgenstern et al., 2007; Séjourné et al., 2011). However, the distribution of the high concentration of scallops from 45°–48°N is not correlated with slopes where enhanced insolation could have increased sublimation. Additionally, there is no evidence of enhanced eolian activity (e.g., dunes, eolian erosional grooves such as yardangs, or eolian deflation hollows) or local difference in albedo that would increase the sublimation rate.

The second hypothesis suggests that the more severe thermokarst between ~38°N and 47°N than in other areas is due initially to a higher content of excess ice. In this latitude range, the 100-m polygons show a remarkably similar morphology (shape and size) and degradation level (polygon junction pits), suggesting that the ice content of wedges was consistent over a large area. On Earth, the depth of thermokarst lakes is controlled by the amount and distribution of ground ice in the substrate (Jorgenson et al., 2010; Soloviev, 1973). Based on this comparison, the largest scallops between ~45°N and 47°N (which are up to 70 m deep) show that the ice-rich zone must be of similar thickness and of relatively high excess ice content (Dundas et al., 2015; Séjourné et al., 2012). This interpretation is in agreement with the observation of a deposit 80 m thick (Figure 6c). At latitudes $<$48°N in UP, the subsurface ice concentration detected by neutron and gamma ray data is significantly lower ($<$4% per weight of ice) than at other latitudes (Feldman et al., 2004; Maurice et al., 2011). However, both of those methods detect hydrogen present at depths less than 1 m, so if the ice is buried deeper, then it would not be detected.

Previous SHARAD studies suggested the presence of an ice-rich layer about 100 m thick (estimated to be 50–85% water ice by volume) in a zone (70°–90°E and 40°–48°N) in the southwestern portion of our study area (Stuurman et al., 2016). We used SHARAD radar detections for our mapping survey (blue and green tracks on Figure 2o). At midlatitudes (39°–45°N), we found a thick deposit of material that corresponds to the ice-rich zone highlighted by our mapping. By using the estimated thickness of 80–100 m, we determined that the material has a dielectric constant between 3.4 and 5.3 (Figure S4). These values are consistent with a material that is primarily ice (~50–85% by volume) with some lithic components. We selected a zone where no extensive sublimation occurred to better estimate the ice content, but a better estimation of the maximum thickness of the deposit would improve that range. Radar reflections are not detected in the zone of significant and deep thermokarst (numerous large- and medium-sized scallops at 45°–47°N; Figure 2o). This absence is either because the physical interfaces do not provide enough dielectric contrast for SHARAD to detect them or in many locations because the ice was sublimated with formation of scallops. It is interesting that we do not see more radar reflections at high latitudes where the LDM is supposedly widespread and visually thick (Figure 2o). We infer either that the radar is unable to penetrate deeply enough to find the interfaces with the underlying basement or that the top and bottom of the ground ice is too close to the surface. SHARAD has a minimum first detection of ~15 m, so the ice must be at depths greater than 15 m to be detected. One other deposit that we detected is associated with the low-latitude assemblage of landforms at about 32°N, but we did not constrain its dielectric properties (Figure 2o).

Mars Advanced Radar for Subsurface and Ionosphere Sounding also detected ground ice at depths down to 60–80 m, probably in the form of excess ice (estimated to be 60% water ice by volume) in UP for latitudes $>$40°N (Mouginot et al., 2012). Therefore, all of these observations are consistent with an interpretation of a thick deposit (at least 80 m) containing excess ice (~50–85% by volume) between ~38°N and 47°N. Presence of ground ice at depth is possible at those latitudes if covered by a dry insulating layer (Bramson et al., 2017; Chamberlain & Boynton, 2007; Mellon et al., 2004).

For latitudes $>$47°N, we suggest that the shallow thermokarst may indicate either a smaller content of excess ice of this midlatitude deposit or, a more recent and less extensive degradation of the LDM than at midlatitudes. The deposition of a thinner LDM at these midlatitudes ($>$47°N from the observation of low-definition CCF, Figure 3d) in UP may have prevented extensive sublimation. Textured terrains are thought to indicate debris-covered, ice-rich LDM (Kreslavsky & Head, 2002b; Mellon et al., 2008). In this context, the occurrence of scallops only on pedestal and lobate ejecta craters around 58°–60°N can be interpreted as the excavation of deep ground ice by impact. It is unclear whether the impacts have excavated the ground ice from the LDM, the deeper ice-rich deposit, or both.

## 6. Discussion: UP, a Case Study of Multiple Depositions of Ice-Rich Sediments Over the Late Amazonian

Our results show that UP is covered by an ice-rich deposit (40–80 m in thickness) of about 11 Ma ages from ~38°N to 47°N which, in turn, is covered by the ice-rich LDM of ~1.5-Ma age for latitudes >47°N. The origin of this midlatitude ice-rich deposit can be tied to obliquity-driven climate changes like the young LDM. The crater retention age indicates a formation during a period of high and moderate obliquity (35° to 45°; Laskar et al., 2004). Formation related to midlatitude glacial land systems along the dichotomy, which is also thought to have formed during moderate (~35°) obliquity periods (Head et al., 2006; Madeleine et al., 2009), has been previously suggested (Séjourné et al., 2012; Soare et al., 2012; Stuurman et al., 2016). The crater retention ages of these glacial features range between ~60 Ma and 1 Ga (Berman et al., 2015; Head et al., 2006; Mangold, 2003; Morgan et al., 2009), and the associated CCF in UP are estimated to be ~60–300 Ma in age (Levy et al., 2009b,; Levy, Head et al., 2010). The difference in crater retention age between these features and the youngest deposition in UP dismisses a related origin. Given the 1.1-Ga age of the older cratered basement, which is a lower bracket on deposition in UP, a related origin cannot be ruled out for older, deeper deposit.

We suggest that this midlatitude ice-rich deposit has the geological characteristics of a stratified sediment not a debris-covered ice sheet such as the LDM. The scallops reveal a complex stratification of the deposit whose origin can be fluvial or eolian (Séjourné et al., 2012). The relative smoothing of topography at midlatitudes (Morgenstern et al., 2007) and absence of layers on crater walls and flow-related stratigraphic landforms support an eolian origin (Soare et al., 2015).

Finally, the surface material in UP may be composed of different sedimentary deposits with various excess ice contents and ages, similar to the ice-rich sedimentary permafrost (Yedoma deposits) on Earth. Underneath the midlatitude ice-rich sediments, the VBF may also contain ice (Clifford & Parker, 2001; Mouginot et al., 2012). Formation of the thick ice-rich Yedoma deposits in the Arctic resulted from the deposition of sediments of different origins (alluvial, eolian, and lacustrine) in a stable nonglaciated region under cold climate conditions over a long period of time (French, 2007). UP appears to be a region of combined depositions of sediment and continuous cold climatic conditions that leaded to a complex distribution of ground ice due to morphoclimatic legacies (marine, fluvial, glacial, or eolian deposition) of the region.

## 7. Conclusion

Our mapping highlighted three assemblages of landforms based on their association at regional and local scales as well as correlation with latitude and topographic roughness at 600-m scale:

1. A high-latitude assemblage composed of mantled deposits, textured terrains, small-sized scallops, and 20- to 50-m-diameter polygons between ~47°N and 78°N. This assemblage is related to the ice-rich, debris-covered, LDM and about 1.5 Ma in age.
2. A midlatitude assemblage including scallops, 100-m-diameter polygons, polygon-junction pits, and mantled deposit that is present from ~38°N to 47°N. This assemblage and SHARAD detection provide evidence for an ice-rich stratified sedimentary permafrost of 80 m in thickness containing excess ice (~50–85% by volume) and about 11 Ma in age.
3. A low-latitude assemblage formed of kilometer-scale polygons, high-albedo mounds, and thumbprint terrains that occurs between ~30°N and 38°N. This assemblage is associated with a lobate deposit of 30 m in thickness with an age of 1.1 Ga.

UP appears to be a region of combined deposition of sediment and continuous cold climatic conditions that led to the formation of thick, stratified, ice-rich deposits, many of which are partially preserved. Future work will focus on extending the grid mapping longitudinally in UP.

**Acknowledgments**
This work is a joint effort of an international team sponsored by the International Space Science Institute (ISSI). Image credits from NASA/JPL/University of Arizona. The authors are funded by the Programme National de Planétologie of the Institut National des Sciences de l'Univers, and the National Science Centre Poland (Narodowe Centrum Nauki) Grant UMO-2013/08/S/ST10/00586. The derived data products are available at https://doi.org/10.5281/zenodo.1404142 (Séjourné, 2018). We thank Rossman P. Irwin III and Michael Zanetti for detailed reviews that improved the manuscript.

## References

Baker, V. R., Strom, R. G., Gulick, V. C., Kargel, J. S., Komatsu, G., & Kale, V. S. (1991). Ancient oceans, ice sheets and the hydrological cycle on Mars. *Nature*, *352*(6336), 589–594. https://doi.org/10.1038/352589a0

Berman, D. C., Crown, D. A., & Joseph, E. C. S. (2015). Formation and mantling ages of lobate debris aprons on Mars: Insights from categorized crater counts. *Planetary and Space Science*, *111*(June), 83–99. https://doi.org/10.1016/j.pss.2015.03.013

Bramson, M. A., Byrne, S., & Bapst, J. (2017). Preservation of midlatitude ice sheets on Mars. *Journal of Geophysical Research: Planets*, *122*, 2250–2266. https://doi.org/10.1002/2017je005357

Buczkowski, D. L., & McGill, G. E. (2002). Topography within circular grabens: Implications for polygon origin, Utopia Planitia, Mars. *Geophysical Research Letters*, *29*(7), 1155. https://doi.org/10.1029/2001GL014100

Buczkowski, D. L., Seelos, K. D., & Cooke, M. L. (2012). Giant polygons and circular graben in western Utopia basin, Mars: Exploring possible formation mechanisms. *Journal of Geophysical Research*, *117*, E08010. https://doi.org/10.1029/2011JE003934

Burr, D. M., Tanaka, K. L., & Yoshikawa, K. (2009). Pingos on Earth and Mars. *Planetary and Space Science*, *57*(5–6), 541–555. https://doi.org/10.1016/j.pss.2008.11.003

Byrne, S., Dundas, C. M., Kennedy, M. R., Mellon, M. T., McEwen, A. S., Cull, S. C., & Daubar, I. J. (2009). Distribution of mid-latitude ground ice on Mars from new impact craters. *Science*, *325*(5948), 1674–1676. https://doi.org/10.1126/science.1175307

Carr, M. H. (2001). Mars global surveyor observations of Martian fretted terrain. *Journal of Geophysical Research*, *106*(E10), 23,571–23,593. https://doi.org/10.1029/2000JE001316

Carr, M. H., & Head, J. W. (2003). Oceans on Mars: An assessment of the observational evidence and possible fate. *Journal of Geophysical Research*, *108*(E5), 5042. https://doi.org/10.1029/2002JE001963

Cedillo-Flores, Y., Treiman, A. H., Lasue, J., & Clifford, S. M. (2011). $CO_2$ gas fluidization in the initiation and formation of Martian polar gullies. *Geophysical Research Letters*, *38*, L21202. https://doi.org/10.1029/2011GL049403

Chamberlain, M. A., & Boynton, W. V. (2007). Response of Martian ground ice to orbit-induced climate change. *Journal of Geophysical Research*, *112*, E06009. https://doi.org/10.1029/2006JE002801

Chevrier, V., Ostrowski, D. R., & Sears, D. W. G. (2008). Experimental study of the sublimation of ice through an unconsolidated clay layer: Implications for the stability of ice on Mars and the possible diurnal variations in atmospheric water. *Icarus*, *196*(2), 459–476. https://doi.org/10.1016/j.icarus.2008.03.009

Christensen, P. R. (2003). Formation of recent Martian gullies through melting of extensive water-rich snow deposits. *Nature*, *422*(6927), 45–48. https://doi.org/10.1038/Nature01436

Clifford, S. M., & Parker, T. J. (2001). The evolution of the Martian hydrosphere: Implications for the fate of a primordial ocean and the current state of the northern plains. *Icarus*, *154*(1), 40–79. https://doi.org/10.1006/icar.2001.6671

Costard, F., Forget, F., Mangold, N., & Peulvast, J. P. (2002). Formation of recent Martian debris flows by melting of near-surface ground ice at high obliquity. *Science*, *295*(5552), 110–113. https://doi.org/10.1126/science.1066698

Costard, F., & Kargel, J. S. (1995). Outwash plains and thermokarst on Mars. *Icarus*, *114*(1), 93–112. https://doi.org/10.1006/icar.1995.1046

Costard, F., Séjourné, A., Kargel, J., & Godin, E. (2016). Modeling and observational occurrences of near-surface drainage in Utopia Planitia, Mars. *Geomorphology*, *275*(December), 80–89. https://doi.org/10.1016/j.geomorph.2016.09.034

Costard, F., Séjourné, A., Kelfoun, K., Clifford, S. M., Lavigne, F., Di Pietro, I., & Bouley, S. (2017). Modeling tsunami propagation and the emplacement of thumbprint terrain in an early Mars ocean. *Journal of Geophysical Research: Planets*, *122*, 633–649. https://doi.org/10.1002/2016JE005230

Daubar, I., McEwen, A., Byrne, S., Kennedy, M., & Ivanov, B. (2013). The current martian cratering rate. *Icarus*, *225*(1), 506–516. https://doi.org/10.1016/j.icarus.2013.04.009

Dickson, J. L., & Head, J. W. (2009). The formation and evolution of youthful gullies on Mars: Gullies as the late-stage phase of mars' most recent ice age. *Icarus*, *204*(1), 63–86. https://doi.org/10.1016/j.icarus.2009.06.018

Dundas, C. M., Bramson, A. M., Ojha, L., Wray, J. J., Mellon, M. T., Byrne, S., et al. (2018). Exposed subsurface ice sheets in the Martian mid-latitudes. *Science*, *359*(6372), 199–201. https://doi.org/10.1126/science.aao1619

Dundas, C. M., Byrne, S., & McEwen, A. S. (2015). Modeling the development of Martian sublimation thermokarst landforms. *Icarus*, *262*, 154–169. https://doi.org/10.1016/j.icarus.2015.07.033

Farrand, W. H., Gaddis, L. R., & Keszthelyi, L. (2005). Pitted cones and domes on Mars: Observations in Acidalia Planitia and Cydonia Mensae using MOC, THEMIS, and TES data. *Journal of Geophysical Research*, *110*, E05005. https://doi.org/10.1029/2004JE002297

Feldman, W. C., Prettyman, T. H., Maurice, S., Plaut, J. J., Bish, D. L., Vaniman, D. T., & Mellon, M. T. (2004). Global distribution of near-surface hydrogen on Mars. *Journal of Geophysical Research*, *109*, E09006. https://doi.org/10.1029/2003JE002160

Forget, F., Haberle, R. M., Montmessin, F., Levrard, B., & Head, J. W. (2006). Formation of glaciers on Mars by atmospheric precipitation at high obliquity. *Science*, *311*(5759), 368–371. https://doi.org/10.1126/science.1120335

French, H., & Shur, Y. (2010). The principles of Cryostratigraphy. *Earth-Science Reviews*, *101*(3–4), 190–206. https://doi.org/10.1016/j.earscirev.2010.04.002

French, H. M. (2007). In Wiley (Ed.), *The periglacial environment* (3rd ed. p. 458). Chichester, UK: John Wiley. https://doi.org/10.1002/9781118684931

Frey, H., & Jarosewich, M. (1982). Subkilometer Martian volcanoes: Properties and possible terrestrial analogs. *Journal of Geophysical Research*, *87*(B12), 9867–9879. https://doi.org/10.1029/JB087iB12p09867

Haberle, R. M., Murphy, J. R., & Schaeffer, J. (2003). Orbital change experiments with a Mars general circulation model. *Icarus*, *161*(1), 66–89. https://doi.org/10.1016/S0019-1035(02)00017-9

Hartmann, W. K. (2005). Martian cratering 8: Isochron refinement and the chronology of Mars. *Icarus*, *174*, 294–320. https://doi.org/10.1016/j.icarus.2004.11.023

Hartmann, W. K., & Daubar, I. J. (2017). Martian cratering 11. Utilizing decameter scale crater populations to study Martian history. *Meteorite Planet Science*, *52*(3), 493–510. https://doi.org/10.1111/maps.12807

Hartmann, W. K., & Neukum, G. (2001). Cratering chronology and the evolution of Mars. *Space Science Reviews*, *96*(1/4), 165–194. https://doi.org/10.1023/A:1011945222010

Hartmann, W. K., & Werner, S. C. (2010). Martian cratering 10. Progress in use of crater counts to interpret geological processes: Examples from two debris aprons. *Earth and Planetary Science Letters*, *294*(3–4), 230–237. https://doi.org/10.1016/j.epsl.2009.10.001

Hauber, E., Van Gasselt, S., Ivanov, B., Werner, S., Head, J. W., Neukum, G., & Jaumann, R. (2005). Discovery of a flank caldera and very young glacial activity at Hecates Tholus, Mars. *Nature*, *434*(7031), 356–361. https://doi.org/10.1038/Nature03423

Head, J. W., Marchant, D. R., Agnew, M. C., Fassett, C. I., & Kreslavsky, M. A. (2006). Extensive valley glacier deposits in the northern mid-latitudes of Mars: Evidence for Late Amazonian obliquity-driven climate change. *Earth and Planetary Science Letters*, *241*(3–4), 663–671. https://doi.org/10.1016/j.epsl.2005.11.016

Head, J. W., Marchant, D. R., Dickson, J. L., Kress, A. M., & Baker, D. M. (2010). Northern mid-latitude glaciation in the Late Amazonian period of Mars: Criteria for the recognition of debris-covered glacier and valley glacier landsystem deposits. *Earth and Planetary Science Letters*, *294*(3–4), 306–320. https://doi.org/10.1016/j.epsl.2009.06.041

Head, J. W., Mustard, J. F., Kreslavsky, M. A., Milliken, R. E., & Marchant, D. R. (2003). Recent ice ages on Mars. *Nature*, *426*(6968), 797–802. https://doi.org/10.1038/Nature02114

Hiesinger, H., & Head, J. W. (2000). Characteristics and origin of polygonal terrain in southern Utopia Planitia, Mars: Results from Mars Orbiter Laser Altimeter and Mars Orbiter Camera data. *Journal of Geophysical Research*, *105*(E5), 11,999–12,022. https://doi.org/10.1029/1999JE001193

Ivanov, B. A. (2001). Mars/moon cratering rate ratio estimates. *Space Science Reviews*, *96*(1/4), 87–104. https://doi.org/10.1023/A:1011941121102

Ivanov, M. A., Hiesinger, H., Erkeling, G., & Reiss, D. (2014). Mud volcanism and morphology of impact craters in Utopia Planitia on Mars: Evidence for the Ancient Ocean. *Icarus*, *228*(0), 121–140. https://doi.org/10.1016/j.icarus.2013.09.018

Jöns, H.-P. (1986). Arcuate ground undulations, gelifluxion-like features and "front Tori" in the northern lowlands on—Do they indicate? *Lunar and Planetary Science Conference*, *17*, 404–405.

Jorgenson, M., Romanovsky, V., Harden, J., Shur, Y., O'Donnell, J., Schuur, E. G., & Marchenko, S. (2010). Resilience and vulnerability of permafrost to climate change. *Canadian Journal of Forest Research*, *40*(7), 1219–1236. https://doi.org/10.1139/X10-060

Kadish, S. J., & Head, J. W. (2014). The ages of pedestal craters on Mars: Evidence for a late-Amazonian extended period of episodic emplacement of decameters-thick mid-latitude ice deposits. *Planetary and Space Science*, *91*, 91–100. https://doi.org/10.1016/j.pss.2013.12.003

Kargel, J. S., Baker, V. R., Beget, J. E., Lockwood, J. F., Pewe, T. L., Shaw, J. S., & Strom, R. G. (1995). Evidence of ancient continental glaciation in the Martian northern plains. *Journal of Geophysical Research*, *100*(E3), 5351–5368. https://doi.org/10.1029/94JE02447

Kneissl, T., van Gasselt, S., & Neukum, G. (2011). Map-projection-independent crater size-frequency determination in GIS environments—New software tool for ArcGIS. *Planetary and Space Science*, *59*(11-12), 1243–1254. https://doi.org/10.1016/j.pss.2010.03.015

Kreslavsky, M. A., & Head, J. W. (2000). Kilometer-scale roughness of Mars: Results from MOLA data analysis. *Journal of Geophysical Research*, *105*(E11), 26695–26711. https://doi.org/10.1029/2000JE001259

Kreslavsky, M. A., & Head, J. W. (2002a). Fate of outflow channel effluents in the northern lowlands of Mars: The Vastitas Borealis Formation as a sublimation residue from frozen ponded bodies of water. *Journal of Geophysical Research*, *107*(E12), 5121. https://doi.org/10.1029/2001JE001831

Kreslavsky, M. A., & Head, J. W. (2002b). Mars: Nature and evolution of young latitude-dependent water-ice-rich mantle. *Geophysical Research Letters*, *29*(15), 1719. https://doi.org/10.1029/2002GL015392

Laskar, J., Correia, A. C. M., Gastineau, M., Joutel, F., Levrard, B., & Robutel, P. (2004). Long term evolution and chaotic diffusion of the insolation quantities of Mars. *Icarus*, *170*(2), 343–364. https://doi.org/10.1016/j.Icarus.2004.04.005

Law, J., & Van Dijk, D. (1994). Sublimation as a geomorphic process: A review. *Permafrost and Periglacial Processes*, *5*(4), 237–249. https://doi.org/10.1002/ppp.3430050404

Lefort, A., Russell, P. S., Thomas, N., McEwen, A. S., Dundas, C. M., & Kirk, R. L. (2009). Observations of periglacial landforms in Utopia Planitia with the High Resolution Imaging Science Experiment (HiRISE). *Journal of Geophysical Research*, *114*, E04005. https://doi.org/10.1029/2008JE003264

Levrard, B., Forget, F., Montmessin, F., & Laskar, J. (2004). Recent ice-rich deposits formed at high latitudes on Mars by sublimation of unstable equatorial ice during low obliquity. *Nature*, *431*(7012), 1072–1075. https://doi.org/10.1038/Nature03055

Levy, J. S., Head, J. W., & Marchant, D. R. (2009a). Thermal contraction crack polygons on Mars: Classification, distribution, and climate implications from HiRISE observations. *Journal of Geophysical Research*, *114*, E01007. https://doi.org/10.1029/2008JE003273

Levy, J. S., Head, J. W., & Marchant, D. R. (2009b). Concentric crater fill in Utopia Planitia: History and interaction between glacial brain-terrains and periglacial mantle processes. *Icarus*, *202*(2), 462–476. https://doi.org/10.1016/j.Icarus.2009.02.018

Levy, J. S., Head, J. W., & Marchant, D. R. (2010). Concentric crater fill in the northern mid-latitudes of Mars: Formation processes and relationships to similar landforms of glacial origin. *Icarus*, *209*(2), 390–404. https://doi.org/10.1016/j.icarus.2010.03.036

Levy, J. S., Marchant, D. R., & Head, J. W. (2010). Thermal contraction crack polygons on Mars: A synthesis from HiRISE, Phoenix, and terrestrial analog studies. *Icarus*, *114*(E1), 229–252. https://doi.org/10.1029/2008JE003273

Madeleine, J.-B., Forget, F., Head, J. W., Levrard, B., Montmessin, F., & Millour, E. (2009). Amazonian northern mid-latitude glaciation on Mars: A proposed climate scenario. *Icarus*, *203*(2), 390–405. https://doi.org/10.1016/j.icarus.2009.04.037

Malin, M. C., Bell, J. F., Cantor, B. A., Caplinger, M. A., Calvin, W. M., Clancy, R. T., & Edgett, K. S. (2007). Context Camera Investigation on board the Mars Reconnaissance Orbiter. *Journal of Geophysical Research*, *112*, E05S04. https://doi.org/10.1029/2006JE002808

Malin, M. C., & Edgett, K. S. (2000). Evidence for recent groundwater seepage and surface runoff on Mars. *Science*, *288*(5475), 2330–2335. https://doi.org/10.1126/Science.288.5475.2330

Malin, M. C., & Edgett, K. S. (2001). Mars Global Surveyor Mars Orbiter Camera: Interplanetary cruise through primary mission. *Journal of Geophysical Research*, *106*(E10), 23429–23570. https://doi.org/10.1029/2000JE001455

Malin, M. C., Edgett, K. S., Posiolova, L. V., McColley, S. M., & Noe Dobrea, E. Z. (2006). Present-day impact cratering rate and contemporary gully activity on Mars. *Science*, *314*(5805), 1573–1577. https://doi.org/10.1126/science.1135156

Mangold, N. (2003). Geomorphic analysis of lobate debris aprons on Mars at Mars Orbiter Camera scale: Evidence for ice sublimation initiated by fractures. *Journal of Geophysical Research*, *108*(E4), 8021. https://doi.org/10.1029/2002JE001885

Mangold, N. (2005). High latitude patterned grounds on Mars: Classification, distribution and climatic control. *Icarus*, *174*(2), 336–359. https://doi.org/10.1016/j.icarus.2004.07.030

Mangold, N. (2011). Ice sublimation as a geomorphic process: A planetary perspective. *Geomorphology*, *126*(1–2), 1–17. https://doi.org/10.1016/j.geomorph.2010.11.009

Maurice, S., Feldman, W., Diez, B., Gasnault, O., Lawrence, D. J., Pathare, A., & Prettyman, T. (2011). Mars odyssey neutron data: 1. Data processing and models of water-equivalent-hydrogen distribution. *Journal of Geophysical Research*, *116*, E11008. https://doi.org/10.1029/2011JE003810

McEwen, A. S., Eliason, E. M., Bergstrom, J. W., Bridges, N. T., Hansen, C. J., Delamere, W. A., & Grant, J. A. (2007). Mars Reconnaissance Orbiter's High Resolution Imaging Science Experiment (HiRISE). *Journal of Geophysical Research*, *112*, E05S02. https://doi.org/10.1029/2005JE002605

McGill, G. E. (1989). Buried topography of Utopia, Mars: Persistence of a giant impact depression. *Journal of Geophysical Research*, *94*(B3), 2753–2759. https://doi.org/10.1029/JB094iB03p02753

McGowan, E. M. (2011). The Utopia/Isidis overlap: Possible conduit for mud volcanism on Mars. *Icarus*, *212*(2), 622–628. https://doi.org/10.1016/j.icarus.2011.01.025

Mellon, M. T., Arvidson, R. E., Marlow, J. J., Phillips, R. J., & Asphaug, E. (2008). Periglacial landforms at the Phoenix landing site and the northern plains of Mars. *Journal of Geophysical Research*, *113*, E00A23. https://doi.org/10.1029/2007JE003039

Mellon, M. T., Arvidson, R. E., Sizemore, H. G., Searls, M. L., Blaney, D. L., & Cull, S., Hecht, M. H. (2009). Ground ice at the Phoenix landing site: Stability state and origin. *Journal of Geophysical Research*, *114*, E00E07. https://doi.org/10.1029/2009JE003417

Mellon, M. T., Feldman, W. C., & Prettyman, T. H. (2004). The presence and stability of ground ice in the southern hemisphere of Mars. *Icarus*, *169*(2), 324–340. https://doi.org/10.1016/j.icarus.2003.10.022

Mellon, M. T., & Jakosky, B. M. (1995). The distribution and behavior of Martian ground ice during past and present epochs. *Journal of Geophysical Research*, *100*(E6), 11,781–11,799. https://doi.org/10.1029/95JE01027

Michael, G. G. (2013). Planetary surface dating from crater size-frequency distribution measurements: Multiple resurfacing episodes and differential isochron fitting. *Icarus*, *226*(1), 885–890. https://doi.org/10.1016/j.icarus.2013.07.004

Mischna, M. A., Richardson, M. I., Wilson, R. J., & McCleese, D. J. (2003). On the orbital forcing of Martian water and $CO_2$ cycles: A general circulation model study with simplified volatile schemes. *Journal of Geophysical Research*, *108*(E6), 5062. https://doi.org/10.1029/2003JE002051

Morgan, G. A., Head, J. W., & Marchant, D. R. (2009). Lineated valley fill (LVF) and lobate debris aprons (LDA) in the Deuteronilus Mensae northern dichotomy boundary region, Mars: Constraints on the extent, age and episodicity of Amazonian glacial events. *Icarus*, *202*(1), 22–38. https://doi.org/10.1016/j.icarus.2009.02.017

Morgenstern, A., Hauber, E., Reiss, D., van Gasselt, S., Grosse, G., & Schirrmeister, L. (2007). Deposition and degradation of a volatile-rich layer in Utopia Planitia and implications for climate history on Mars. *Journal of Geophysical Research*, *112*, E06010. https://doi.org/10.1029/2006JE002869

Mouginot, J., Pommerol, A., Beck, P., Kofman, W., & Clifford, S. M. (2012). Dielectric map of the Martian northern hemisphere and the Nature of plain filling materials. *Geophysical Research Letters*, *39*, L02202. https://doi.org/10.1029/2011GL050286

Musselwhite, D. S., Swindle, T. D., & Lunine, J. I. (2001). Liquid $CO_2$ breakout and the formation of recent small gullies on Mars. *Geophysical Research Letters*, *28*(7), 1283–1285. https://doi.org/10.1029/2000GL012496

Mustard, J. F., Cooper, C. D., & Rifkin, M. K. (2001). Evidence for recent climate change on Mars from the identification of youthful near-surface ground ice. *Nature*, *412*(6845), 411–414. https://doi.org/10.1038/35086515

Orgel, C., Hauber, E., van Gasselt, S., Reiss, D., Johnsson, A., Ramsdale, J. D., & Swirad, Z. M. (2018). Grid-mapping of the Northern Plains of Mars: A new overview of recent ice-related landforms in Acidalia Planitia. *Journal of Geophysical Research: Planets*, *123*. https://doi.org/10.1029/2018JE005664

Parker, T. J., Gorsline, D. S., Saunders, R. S., Pieri, D. C., & Schneeberger, D. M. (1993). Coastal geomorphology of the Martian northern plains. *Journal of Geophysical Research*, *98*(E6), 11061–11,078. https://doi.org/10.1029/93JE00618

Pechmann, J. C. (1980). The origin of polygonal troughs on the northern plains of Mars. *Icarus*, *42*(2), 185–210. https://doi.org/10.1016/0019-1035(80)90071-8

Pelletier, J. D., Kolb, K. J., McEwen, A. S., & Kirk, R. L. (2008). Recent bright gully deposits on Mars: Wet or dry flow? *Geology*, *36*(3), 211–214. https://doi.org/10.1130/G24346A.1

Pike, R. J. (1977). Size-dependence in the shape of fresh impact craters on the Moon. In D. J. Roddy, R. O. Pepin, & R. B. Merrill (Eds.), *Impact and explosion cratering*, (pp. 489–509). New York: Pergamon Press.

Platz, T., Michael, G., Tanaka, K. L., Skinner, J. A., & Fortezzo, C. M. (2013). Crater-based dating of geological units on Mars: Methods and application for the new global geological map. *Icarus*, *225*(1), 806–827. https://doi.org/10.1016/j.icarus.2013.04.021

Plaut, J. J., Safaeinili, A., Holt, J. W., Phillips, R. J., Head, J. W., Seu, R., et al. (2009). Radar evidence for ice in lobate debris aprons in the mid-northern latitudes of Mars. *Geophysical Research Letters*, *36*, L02203. https://doi.org/10.1029/2008GL036379

Plescia, J. B. (1990). Recent flood lavas in the Elysium region of Mars. *Icarus*, *88*(2), 465–490. https://doi.org/10.1016/0019-1035(90)90095-Q

Rampton, V. N. (1974). The influence of ground ice and thermokarst upon the geomorphology of the Mackenzie-Beaufort region. In B. D. Fahey, & R. D. Thompson (Eds.), *Research in polar and alpine geomorphology*, *Guelph symposium on geomorphology* (3rd ed., pp. 43–59). Norwich: Geo Abstracts Ltd.

Ramsdale, J. D., Balme, M. R., Conway, S. J., Gallagher, C., van Gasselt, S. A., Hauber, E., et al. (2017). Grid-based mapping: A method for rapidly determining the spatial distributions of small features over very large areas. *Planetary and Space Science*, *140*(Supplement C), 49–61. https://doi.org/10.1016/j.pss.2017.04.002

Ramsdale, J. D., Balme, M. R., Gallagher, C., Conway, S. J., Smith, I. B., Hauber, E., & Orgel, C. (2018). Gridmapping the northern plains of Mars: Geomorphological, radar and water-equivalent hydrogen results from Arcadia Plantia suggest possible fluvial and volcanic systems overlain by a ubiquitous and heavily degraded ice-rich latitude-dependent mantle. *Journal of Geophysical Research: Planets*, *123*. https://doi.org/10.1029/2018JE005663

Rodriguez, J. A. P., Fairen, A. G., Tanaka, K. L., Zarroca, M., Linares, R., Platz, T., & Komatsu, G. (2016). Tsunami waves extensively resurfaced the shorelines of an early Martian ocean. *Scientific Reports*, *6*(1), 25,106. https://doi.org/10.1038/srep25106

Schon, S. C., Head, J. W., & Fassett, C. I. (2012). Recent high-latitude resurfacing by a climate-related latitude-dependent mantle: Constraining age of emplacement from counts of small craters. *Planetary and Space Science*, *69*(1), 49–61. https://doi.org/10.1016/j.pss.2012.03.015

Seibert, N. M., & Kargel, J. S. (2001). Small-scale Martian polygonal terrain: Implications for liquid surface water. *Geophysical Research Letters*, *28*(5), 899–902. https://doi.org/10.1029/2000GL012093

Séjourné, A. (2018). Distribution of water- and ice-related landforms in Utopia Planitia, Mars [data set]. *Zenodo*. https://doi.org/10.5281/zenodo.1404143

Séjourné, A., Costard, F., Gargani, J., Soare, R. J., Fedorov, A., & Marmo, C. (2011). Scalloped depressions and small-sized polygons in Western Utopia Planitia, Mars: A new formation hypothesis. *Planetary and Space Science*, *59*(5–6), 412–422. https://doi.org/10.1016/j.pss.2011.01.007

Séjourné, A., Costard, F., Gargani, J., Soare, R. J., & Marmo, C. (2012). Evidence of an Eolian ice-rich and stratified permafrost in Utopia Planitia, Mars. *Planetary and Space Science*, *60*(1), 248–254. https://doi.org/10.1016/j.pss.2011.09.004

Skinner, J. A., & Mazzini, A. (2009). Martian mud volcanism: Terrestrial analogs and implications for formational scenarios. *Marine and Petroleum Geology*, *26*(9), 1866–1878. https://doi.org/10.1016/j.marpetgeo.2009.02.006

Skinner, J. A., Tanaka, K. L., & Platz, T. (2012). Widespread loess-like deposit in the Martian northern lowlands identifies middle Amazonian climate change. *Geology*, *40*(12), 1127–1130. https://doi.org/10.1130/G33513.1

Smith, D., Neumann, G., Arvidson, R. E., Guinness, E. A., & Slavney, S. (2003). Mars Global Surveyor laser altimeter mission experiment gridded data record. NASA Planetary Data System, MGS-M-MOLA-5-MEGDR-L3-V1.0.

Smith, D. E., Zuber, M. T., Frey, H. V., Garvin, J. B., Head, J. W., Muhleman, D. O., et al. (2001). Mars Orbiter Laser Altimeter: Experiment summary after the first year of global mapping of Mars. *Journal of Geophysical Research*, *106*(E10), 23689–23722. https://doi.org/10.1029/2000JE001364

Smith, I. B., & Holt, J. W. (2015). Spiral trough diversity on the north pole of Mars, as seen by Shallow Radar (SHARAD). *Journal of Geophysical Research: Planets*, *120*, 362–387. https://doi.org/10.1002/2014je004720

Soare, R. J., Burr, D. M., & Wan Bun Tseung, J. M. (2005). Possible pingos and a periglacial landscape in northwest Utopia Planitia. *Icarus*, *174*(2), 373–382. https://doi.org/10.1016/j.icarus.2004.11.013

Soare, R. J., Conway, S. J., Pearce, G. D., Costard, F., & Séjourné, A. (2013). Sub-kilometre (intra-crater) mounds in Utopia Planitia, Mars: Character, occurrence and possible formation hypotheses. *Icarus*, *225*(2), 982–991. https://doi.org/10.1016/j.Icarus.2012.06.003

Soare, R. J., Costard, F., Pearce, G. D., & Séjourné, A. (2012). A re-interpretation of the recent Stratigraphical history of Utopia Planitia, Mars: Implications for late-Amazonian periglacial and ice-rich terrain. *Planetary and Space Science*, *60*(1), 131–139. https://doi.org/10.1016/j.pss.2011.07.007

Soare, R. J., Horgan, B., Conway, S. J., Souness, C., & El-Maarry, M. R. (2015). Volcanic terrain and the possible periglacial formation of excess ice at the mid-latitudes of Utopia Planitia, Mars. *Earth and Planetary Science Letters*, *423*(August), 182–192. https://doi.org/10.1016/j.epsl.2015.04.033

Soare, R. J., Kargel, J. S., Osinski, G. R., & Costard, F. (2007). Thermokarst processes and the origin of crater-rim gullies in Utopia and western Elysium Planitia. *Icarus*, *191*(1), 95–112. https://doi.org/10.1016/j.icarus.2007.04.018

Soare, R. J., Osinski, G. R., & Roehm, C. L. (2008). Thermokarst lakes and ponds on Mars in the very recent (late Amazonian) past. *Earth and Planetary Science Letters*, *272*(1–2), 382–393. https://doi.org/10.1016/j.epsl.2008.05.010

Soare, R. J., Séjourné, A., Pearce, G. D., Costard, F., & Osinski, G. R. (2011). The Tuktoyaktuk Coastlands of northern Canada: A possible "wet" periglacial analogue of Utopia Planitia, Mars. *Geological Society of America Special Papers*, *483*, 203–218. https://doi.org/10.1130/2011.2483(13)

Soloviev, P. A. (1973). Thermokarst phenomena and landforms due to frost heaving in central Yakutia. *Biuletyn Peryglacjalny*, *23*, 135–155.

Souness, C., Hubbard, B., Milliken, R. E., & Quincey, D. (2012). An inventory and population-scale analysis of Martian glacier-like forms. *Icarus*, *217*(1), 243–255. https://doi.org/10.1016/j.Icarus.2011.10.020

Squyres, S. W. (1978). Martian fretted terrain: Flow of erosional debris. *Icarus*, *34*(3), 600–613. https://doi.org/10.1016/0019-1035(78)90048-9

Squyres, S. W. (1979). The distribution of lobate debris aprons and similar flows on Mars. *Journal of Geophysical Research*, *84*(B14), 8087–8096. https://doi.org/10.1029/JB084iB14p08087

Stuurman, C. M., Osinski, G. R., Holt, J. W., Levy, J. S., Brothers, T. C., Kerrigan, M., & Campbell, B. A. (2016). SHARAD detection and characterization of subsurface water ice deposits in Utopia Planitia, Mars. *Geophysical Research Letters*, *43*, 9484–9491. https://doi.org/10.1002/2016GL070138

Tanaka, K. L., Skinner, J. A., Dohm, J. M., Irwin, R. P., Kolb, E. J., Fortezzo, C. M., et al. (2014). Geologic map of Mars: Scale 1:20,000,000, US Geol. Surv. Sci. Invest. Map 3292 pamphlet 43 p. https://doi.org/10.3133/sim3292.

Tanaka, K. L., Skinner, J. A., & Hare, T. M. (2005). Geologic map of the northern plains of Mars, scale 1:15,000,000. US Geol. Surv. Sci. Invest. Map 2888.

Thomson, B. J., & Head, J. W. (2001). Utopia Basin, Mars: Characterization of topography and morphology and assessment of the origin and evolution of basin internal structure. *Journal of Geophysical Research*, *106*(E10), 23209–23230. https://doi.org/10.1029/2000JE001355

Treiman, A. H. (2003). Geologic settings of Martian gullies: Implications for their origins. *Journal of Geophysical Research*, *108*(E4), 8031. https://doi.org/10.1029/2002JE001900

Ulrich, M., Hauber, E., Herzschuh, U., Hartel, S., & Schirrmeister, L. (2011). Polygon pattern Geomorphometry on Svalbard (Norway) and Western Utopia Planitia (Mars) using high-resolution stereo remote-sensing data. *Geomorphology*, *134*(3-4), 197–216. https://doi.org/10.1016/j.geomorph.2011.07.002

Ulrich, M., Morgenstern, A., Gunther, F., Reiss, D., Bauch, K. E., Hauber, E., et al. (2010). Thermokarst in Siberian ice-rich permafrost: Comparison to asymmetric scalloped depressions on Mars. *Journal of Geophysical Research*, *115*, E10009. https://doi.org/10.1029/2010JE003640

Van Dijk, D., & Law, J. (1995). Sublimation and aeolian sand movement from a frozen surface: Experimental results from Presqu'ile beach, Ontario. *Geomorphology*, *11*(3), 177–187. https://doi.org/10.1016/0169-555X(94)00065-Y

Van Everdingen, R. (1998). *Multi-language glossary of permafrost and related ground-ice terms*. Revised May 2005. Boulder, CO: National Snow; Ice Data Center.

Voelker, M., Hauber, E., Schulzeck, F., & Jaumann, R. (2017). Grid-mapping Hellas Planitia, Mars—Insights into distribution, evolution and geomorphology of (Peri)-glacial, fluvial and lacustrine landforms in Mars' deepest basin. *Planetary and Space Science*, *145*(Supplement C), 49–70. https://doi.org/10.1016/j.pss.2017.07.012

Warner, N. H., Gupta, S., Calef, F., Grindrod, P., Boll, N., & Goddard, K. (2015). Minimum effective area for high resolution crater counting of Martian terrains. *Icarus*, *245*(January), 198–240. https://doi.org/10.1016/j.icarus.2014.09.024

Werner, S. C., Tanaka, K. L., & Skinner, J. A. (2011). Mars: The evolutionary history of the northern lowlands based on crater counting and geologic mapping. *Planetary and Space Science*, *59*(11–12), 1143–1165. https://doi.org/10.1016/j.pss.2011.03.022

Zanetti, M., Hiesinger, H., Reiss, D., Hauber, E., & Neukum, G. (2010). Distribution and evolution of scalloped terrains in the southern hemisphere. Mars. *Icarus*, *206*(2), 691–706. https://doi.org/10.1016/j.icarus.2009.09.010